Journal of Catalysis 450 (2025) 116313

Contents lists available at ScienceDirect

Journal of Catalysis

journal homepage: www.elsevier.com/locate/jcat

Research article

DFT+U calculations on substitutionally doped (Ni, Cu, Zn) Mg-vanadate surfaces for the oxidative dehydrogenation of alkanes

Hansel Montalvo-Castro [a,b], Siby Thomas [a], Randall J. Meyer [c], David Hibbitts [a,d,*]

[a] Department of Chemical Engineering, University of Florida, Gainesville, FL 32611, United States
[b] Department of Chemical Engineering, University of Puerto Rico-Mayagüez, Mayagüez, PR 00681, United States
[c] ExxonMobil Technology and Engineering Company, Annandale, NJ 08801, United States
[d] Davidson School of Chemical Engineering, Purdue University, West Lafayette, IN 47907, United States

ARTICLE INFO

Keywords:
Oxidative dehydrogenation
Magnesium vanadates
Dopants
C–H activation

ABSTRACT

Mg-vanadate ($Mg_xV_2O_{x+5}$) catalysts are promising materials for selectively converting alkanes into desired alkenes during oxidative dehydrogenation (ODH) reactions. Here, we employ density functional theory (DFT+U) calculations, to explore Ni, Cu, and Zn doped substitutionally into Mg positions in Mg-vanadate surfaces for the initial C–H activation of ethane, chosen here as a simple probe reactant. Cation exchange energies to replace the Mg^{2+} with a dopant are not strongly sensitive to changes in the Mg-V ratio, but exchange was more favorable into less-coordinated Mg-sites (i.e., those near surfaces). We examined the reducibility of 54 distinct O atoms on 12 distinct Mg-vanadate catalysts by calculating hydrogen addition energies (HAE), methyl-addition energies (MAE), and ethane C–H activation barriers. Our results show that dopants modulate surface reactivity by making unreactive O atoms (in undoped surfaces) more reactive upon doping, while already reactive O atoms retain similar reactivity, as modulated by whether the dopants are reduced, or V is reduced. Zn is rarely reduced in our calculations (~8% of cases), and as such Zn has a minor impact, on average, on the HAE, MAE, and C–H activation barriers. Cu, in contrast, reduces ~80 % of the time, resulting in large increases in surface reducibility (decreases in the values of HAE, MAE, and C–H activation barriers). Ni is less likely than Cu to be reduced, and more likely than Zn, resulting in intermediate behavior. When these dopants do not reduce, dopants can still have smaller impacts on the reactivity of nearby O atoms, but the average shifts in reducibility are negligible, suggesting that the impact of their exchange is less predictable in situations that they do not become reduction centers. These results give insights into the role of altering or mixing divalent cations in metal-vanadate catalysts.

1. Introduction

Light alkanes such as methane (CH_4), ethane (C_2H_6), and propane (C_3H_8) are attractive hydrocarbon feedstocks for the synthesis of value-added products. These alkanes are relatively abundant and found in non-conventional fossil fuel sources, such as shale gas, biogenic sources, and decaying organic matter [1–3]. Alkanes, however, are relatively unreactive, often attributed to their high-symmetry structures, strong C–H bonds, [4] and high-energy filled orbitals [5]. Current conversion methods that enable difficult C–H bond activation are energy intensive and include fluid-catalytic cracking, [6] steam cracking, [7,8] and catalytic dehydrogenation reactions [9–11]. These processes, however, are often limited by thermodynamic constraints and practical challenges such as the formation of coke at high temperatures [12,13]. Partial oxidative dehydrogenation (ODH) represents a relatively energy-efficient, exothermic route for producing alkenes from alkanes, with water as a byproduct [14–17]. Alkane ODH is thought to proceed via the Mars-van Krevelen (MvK) mechanism on metal oxide catalysts, [18,19] with the initial alkane C–H bond activation as the rate determining step [20,21]. The ODH reaction, however, is prone to low alkene selectivity because of the formation of undesired CO_x products [14]. Despite the drawbacks of ODH, it is considered a viable alternative to catalytic cracking and dehydrogenation techniques because it overcomes the equilibrium limitations of non-oxidative dehydrogenation [22].

Vanadium-based metal oxide catalysts [23–25] have been reported as superior candidates for the ODH reaction [26] of alkanes. These materials exhibit relatively large surface areas and thermal stability, [23] and are among the most active during alkane ODH. V atoms can

---

* Corresponding author at: Davidson School of Chemical Engineering, Purdue University, West Lafayette, IN 47907, United States.
E-mail address: hibbitts@purdue.edu (D. Hibbitts).

https://doi.org/10.1016/j.jcat.2025.116313
Received 9 April 2025; Received in revised form 29 June 2025; Accepted 3 July 2025
Available online 14 July 2025
0021-9517/© 2025 Elsevier Inc. All rights are reserved, including those for text and data mining, AI training, and similar technologies.

occupy different oxidation states in (2^+ to 5^+), [27,28] which in turn allows for varying coordination environments as well as different extents of surface reduction during reaction. For example, the initial C–H activation of alkanes during ODH reaction likely involves a single reduction transition in V (5^+ to 4^+) to accommodate homolytically cleaved H (radical like) on a lattice O atom. Kinetic studies on ethane and propane ODH reveal that the selectivity toward the desired alkene is higher on dispersed VO_x species compared to extended V_2O_5 surfaces and clusters, as varied through VO_x weight loading [25,29–37]. For example, at low VO_x loadings on supports, isolated and thus dispersed VO_4 species are formed [29,38–40]. With increasing vanadium loading, the surface configuration evolves from isolated to dimeric and trimeric vanadates, eventually forming vanadia (V_2O_5) clusters. Among these, isolated VO_x species exhibit higher selectivity, but lower activity compared to polymeric VO_x and crystalline V_2O_5. Additional VO_x-based catalysts have been studied, such as polyoxometalates (POMs, e.g., $H_4PV_1W_{11}O_{40}$) [4] and mixed metal oxides ($MoVTeNbO_x$) [41,42]. These catalysts exhibit isolated VO_x species in their corresponding crystal lattice. In addition to POMs and the M1 phase oxides, other mixed metal oxide vanadates have been studied for ODH reaction (Table 1), which exhibit varying stoichiometries ($M_xV_yO_z$). The key observation among these materials is that V maintains a formal oxidation state of 5^+ in combination with monovalent, divalent, and trivalent metal cations (M).

Alkali metal vanadates (MVO_3, M: Li, K, Rb, Cs) have been studied for ethane-N_2O reactions, with $LiVO_3$ exhibiting the highest alkene selectivity [19,43]. Alkali metals are unlikely to undergo reduction, thus it is most likely that reduction of V atoms mediates chemistry in alkali metal vanadates. Transition metal vanadates, on the other hand, contain additional reduction centers. Kinetic measurements for butane ODH on MVO_4 (M: Fe, Eu, Cr, Sm, Nd) and $M_3V_2O_8$ orthovanadates (M: Cu, Ni, Zn) (773 K, 4 kPa C_4H_{10}, 8 kPa O_2) showed that $EuVO_4$ had the highest activity. On the other hand, $NdVO_4$ showed the highest selectivity (56 %) and $Cu_3V_2O_8$ showed the lowest (3.5 %) [48]. Among these materials, the more reducible cations exhibited the lower selectivity toward butene and butadiene. However, other correlations between selectivity and surface properties, such as the 1s oxygen biding energy and cation electronegativity were not successful. This motivates the theoretical exploration of oxygen-specific descriptors in Mg-vanadate surfaces [48]. Consistent with our previous work, this suggest that predictions on surface reactivity (and ultimately, selectivity) require considering each distinct O atom, specifically in low-symmetry unit cell surfaces that expose varying lattice O atoms. For the case of propane ODH (673 K, 10–30 kPa C_3H_8, 15–20 kPa O_2) kinetic measurements on rare-earth MVO_4 (M: La, Ce, Pr, Nd, Sm, Tb, Er, Yb) catalysts showed the highest rates for $ErVO_4$ and highest propene selectivity for $NdVO_4$ (42 %), consistent with that of butane ODH, and without correlation to reduction potentials [19,37,49]. Overall, the large configurational design space among these materials of varying stoichiometries render difficult to decouple geometric and electronic effects that in turn mediate ODH rates and selectivities, and thus here we focus on divalent metal vanadates.

Divalent metal vanadates can be synthesized with a range of stoichiometric M:V ratios (i.e., metavanadate, MV_2O_6; pyrovanadate, $M_2V_2O_7$; and orthovanadate, $M_3V_2O_8$), and these have been studied for ODH with varying divalent cations including alkali earth (Mg), transition (Co, Ni, Cu, Zn), and post-transition (Pb) metals [46]. Among these, Mg vanadates have been explored for the ODH of ethane, [50,51] propane, [51–53] butane, [54] 2-methylpropane, [50] and cyclohexane [55]. For example, kinetic measurements for propane ODH (813 K, $C_3H_8/O_2 = 2$) [53] on Mg-vanadate catalysts of varying compositions resulted in propene selectivity up to 65 % (1 % C_3H_8/0.1 % O_2, balance He) at 10 % conversion, which was significantly higher than that of V_2O_5 or MgO catalysts with selectivity 18 % and 33 %, respectively [56,57]. $Mg_3V_2O_8$ catalysts showed superior selectivity (56 %) compared to $Mg_2V_2O_7$ (16 %) and MgV_2O_6 (14 %) for the ODH of butane (813 K, $C_4H_{10}/O_2 = 0.5$), [58] a trend which has been attributed to the effective isolation of VO_x clusters in $Mg_3V_2O_8$ [58]. These Mg-V-O based Mg vanadate catalysts show better activity and selectivity during alkane ODH reaction, outperforming V_2O_5 and supported VO_x catalysts [59]. In addition to their promising kinetics, these Mg-vanadates are fundamentally attractive because they result in a nice set of materials with varying stoichiometries and VO_x geometries, while conserving the overall oxidation states of their constituent atoms ($Mg = 2^+, V = 5^+, O = 2^-$). This, in turn, allows for a direct comparison of the structural features among these materials.

Table 1
Metal vanadates (with V^{5+} cations) used for alkane ODH.

Catalyst	Cations (M)	Refs.
MVO_3	Li^{1+}, K^{1+}, Rb^{1+}, Cs^{1+}	[19,43]
MV_2O_6	Mg^{2+}, Cu^{2+}, Zn^{2+}, Pb^{2+}	[44]
$M_2V_2O_7$	Mg^{2+}, Mn^{2+}, Co^{2+}, Ni^{2+}, Cu^{2+}, Zn^{2+}, Cd^{2+}, Pb^{2+}	[45–47]
$M_3V_2O_8$	Mg^{2+}, Ni^{2+}, Cu^{2+}, Zn^{2+}, Pb^{2+}	[46]
$M_5V_2O_{10}$	Cu^{2+}	[44]
MVO_4	Cr^{3+}, Fe^{3+}, Bi^{3+}, La^{3+}, Ce^{3+}, Pr^{3+}, Nd^{3+}, Sm^{3+}, Eu^{3+}, Tb^{3+}, Er^{3+}, Yb^{3+}	[19,37,48,49]

Our recent DFT+U study examined initial C–H activation of C_1–C_3 alkanes on V_2O_5 and Mg-vanadate catalysts ($M_xV_2O_{5+x}$, $x = 1$–3). Initial C–H activation barriers among the alkanes were shown to correlate with their corresponding C–H bond dissociation energy ($CH_4 > C_2H_6 > C_3H_8$). In addition—when considering the most reactive O-atom per bulk material—initial C–H activation barriers were shown to increase with increasing Mg-content ($V_2O_5 < MgV_2O_6 \sim Mg_2V_2O_7 < Mg_3V_2O_8$), suggesting an activity-selectivity trade off in these systems since catalysts with higher Mg content ($Mg_3V_2O_8$) have been associated with higher alkane ODH selectivity [51,57,60,61]. These initial C–H activation barriers were found to correlate with the corresponding O atom hydrogen addition energy (HAE), as used elsewhere, [4,62–64] and with methyl addition energies (MAE), which outperformed HAE as a descriptor [51]. Additional probes, such as surface formation energy (SFE), vacancy formation energy (VFE), and the O 2p band centers were weak descriptors for initial C–H activation of alkanes [51].

Contrasting different divalent metal vanadates gives insights into how the divalent cation can influence reaction rates and selectivities. For example, when contrasting pyrovanadate ($M_2V_2O_7$; M: Mg, Mn, Cu) catalysts for propane ODH at varying temperatures (673–973 K), $Mg_2V_2O_7$ was shown the most active, while both Cu and Mn pyrovanadate catalysts were more selective toward propene, with $Cu_2V_2O_7$ exhibiting 40 % propene selectivity at 855 K while that for $Mg_2V_2O_7$ was 20 % at 835 K [47]. Another example includes propane ODH on $M_xV_2O_{5+x}$ catalysts (M: Mg, Zn, Pb) that showed that both activity and selectivity decrease in the order of Mg>Pb>Zn (773–823 K, 40 kPa C_3H_8, 20 kPa O_2) [46]. Although the $Pb_xV_2O_{5+x}$ catalysts show comparable selectivities to $Mg_xV_2O_{5+x}$ catalysts, they are thought to be less active because of their lower oxidation potentials [46]. Another study contrasting Cu-vanadates ($Cu_xV_2O_{x+5}$, x = 0, 1, 2, 3, and 5), showed that V_2O_5, CuV_2O_6, and $Cu_2V_2O_7$ were more active compared to $Cu_3V_2O_8$ and $Cu_5V_2O_{10}$ during the anaerobic oxidation of isobutane (573–673 K, 101 kPa, 75 mol% isobutane and 5 mol% O_2), [44] suggesting that activity decreases with increasing Cu:V. This reactivity trend is consistent with our findings on $Mg_xV_2O_{x+5}$, that suggest higher initial C–H activation barriers with increasing Mg:V ratios. Overall, these studies suggest that ODH activity and selectivity can be tuned with the appropriate selection of the divalent atom in metal vanadates. Here, we focus on substitutionally doping Ni, Cu, and Zn into Mg positions in $Mg_xV_2O_{5+x}$ catalysts to understand how these dopants may be leveraged to tune the reactivity of those catalysts to further enhance their performance. Despite the ability to make many divalent metal vanadate structures ($M_xV_2O_{5+x}$, M: Mg, Mn, Co, Ni, Cu, Zn, Pb), no studies have examined the role of dopants in Mg vanadate systems.

Dopants can significantly influence oxide catalyst behaviour by modifying catalytic activity, selectivity, stability, redox properties, and acid-base properties [65]. Dopants alter the electronic structure and surface properties of the catalyst by introducing new active sites, changing adsorption energies, and promoting specific reaction pathways [66]. For example, substitutionally doped CeO_2 (Zr^{4+}, La^{3+}, Eu^{3+}, and Sm^{3+}) surfaces, exhibit changes in the distribution of periodic electrostatic fields relative to pristine CeO_2 counterpart, likely because of the differences in electronegativity, ionic radius, and valence between dopant and Ce atoms. These changes can be geometric (e.g., dopants induce significant lattice distortions), electronic (dopants introduce new reaction sites), or a combination of both. These surface modifications, in turn, change surface reactivity by modulating surface area, formation and stability of oxygen vacancies, and availability of active sites [67]. In addition to these changes, substitutional doping can also modify underlying surface phenomena such as its electrical conductivity and oxygen transport properties, which can also influence catalytic performance, especially for reactions in which electron transfers may be involved [68]. For example, doping CeO_2 catalysts with Pd cations decreased methane activation barriers relative to CeO_2 (1 1 1), PdO (1 0 0), and Pd (1 1 1) counterparts [69]. Similarly, DFT+U calculations on transition metal (Ag, Au, Ni, Co, Pt, Pd, and Mn) doped CeO_2 surfaces exhibited lower methane activation energies, with the dopant either becoming the reduction centre or altering the reducibility of the Ce atoms during C–H bond activation [70]. In addition, La_2O_3 doped with Cu, Mg, or Zn, [71] as well as CeO_2 doped with Pt [72] showed lower alkane C–H activation energies compared to their oxide pristine forms. Incorporation of Sn, Ti, and W dopants into NiO catalysts led to increased stability than pure NiO, and showed an activity and selectivity increase of ~50 % during ethane ODH (473–673 K, 10 kPa C_2H_6 and 5 kPa O_2 in He) [73]. M−doped NiO catalysts (M = Mg, Al, Ga, Ti, Nb) showed that Nb-doped NiO possess superior alkene selectivity (88 %) for the ODH of ethane (673 K, $C_2H_6/O_2 = 1$) compared to Ti-NiO (78 %), Al-NiO (63 %), Ga-NiO (53 %) and pure NiO (20 %) [74].

Here, we employ density functional theory (DFT+U) to investigate the role of Ni, Cu, and Zn as substitutional dopants in Mg-vanadate surfaces on initial alkane C–H activation barriers in ethane. This series of 3d dopants was selected because they can be divalent cations and have been used to synthesize $M_xV_2O_{5+x}$ catalysts for ODH (Table 1) [44–47,51]. Furthermore, these dopants have different affinities for one-electron reduction, with Cu^{2+} being the easiest to reduce while Zn^{2+} is the hardest [75]. Consistent with their single electron reduction affinity, we show that C–H activation barriers for C_2H_6 on Cu-doped Mg vanadates are mediated by Cu reduction, while reductions on undoped [51], Ni- and Zn-doped Mg vanadates are mostly mediated by V reduction. We also show that among Ni, Cu, and Zn substitutional dopants, Cu results in the largest exothermic shifts in HAE, MAE, and C_2H_6 activation barriers. Thus, the introduction of reducible cations into Mg positions can be leveraged to modify activation energies relative to pristine Mg-vanadate counterparts. This increase in reactivity with Cu-doped $M_xV_2O_{5+x}$ catalysts, however, is not expected to increase selectivity (and may decrease it because of the previously observed activity-selectivity trade off), although additional studies are underway to examine selectivity trends among these materials. Overall, this work demonstrates that substitutional dopants on Mg lattice positions in $Mg_xV_2O_{5+x}$ catalysts have the potential for tunning reactivity and selectivity on Mg-vanadates by influencing C–H activation barriers, controlled by the extend of dopant reducibility.

2. Methods

Periodic density functional theory (DFT) calculations were performed using the Vienna ab initio simulation package (VASP) [76,77] as implemented on the Computational Catalysis Interface (CCI) [78]. Structure relaxation and subsequent property calculations were conducted using plane-wave basis sets [79,80] constructed with projector augmented wave (PAW) potentials. The Perdew-Burke-Ernzerhof (PBE) functional, a type of generalized gradient approximation (GGA) method, was employed to account for the exchange and correlation energies [81] with a kinetic energy cut-off of 400 eV for all spin-polarized calculations.

The GGA approach, however, often results in self-interaction errors associated with the partial occupation and delocalization of *d* and *f* orbitals present in transition metal oxides. This leads to an overall overestimation of oxidation energies in the metal oxides [82]. To address this issue, an onsite Coulomb interaction, known as the Hubbard *U*-term, was implemented using the DFT+U approach [83–85]. The DFT+U approach penalizes partial occupation of localized orbitals, reducing electron delocalization and in the present study, the U correction has been included only to the V atoms to mitigate the self-interaction error associated with the partial occupation and delocalization of *d* and *f* orbitals in transition metal-doped Mg-vanadates. However, the choice of the *U* value is not a well-defined entity and is challenging to determine without direct experimental benchmarks. Hence, we adopted a previously reported *U* value of 3.0 eV for V in Mg-vanadates, [82,86–93] shown to correct the otherwise DFT underestimated bandgap (1.6 eV) of V_2O_5 when compared to the experimental bandgap (2.0 eV) [82]. Since the identification of *U* values for Ni, Cu, and Zn is challenging and difficult to benchmark on a Mg-vanadate environment, we chose to not apply U corrections to dopant atoms in the interest of a consistent basis for comparison across the doped surfaces (which would otherwise be biased to the arbitrary selection of the *U* parameter). Lastly, we note that, while experimentally relevant energies require appropriate U corrections, these do not disturb the linear relationships of catalytic reactions including C–H activation, [94] and thus the trends presented in this work do distinguish the relative tendencies of Ni, Cu, and Zn on the reactivity of Mg-vanadate systems.

The surface models in this work were obtained by cleaving the bulk structures (Fig. 1) of the optimized metavanadate (MgV_2O_6), pyrovanadate ($Mg_2V_2O_7$), and orthovanadate ($Mg_3V_2O_8$). The Brillouin zone of the cleaved Mg-vanadate surfaces (Fig. 2) was sampled with varying k-point grids, according to the Γ-centered scheme. Detailed k-point selections for different surface structures presented in this work are provided in our previous work [51]. A vacuum space of 10 Å was used between surface slabs. During surface optimization calculations, the positions of the Mg, V, and O atoms within the bottom half of the slab were held fixed, while top half layers were allowed to relax during optimization.

Gas molecules considered in this study include C_1–C_3 alkanes (CH_4, C_2H_6, and C_3H_8), water (H_2O), and oxygen (O_2). To avoid periodic interactions, gas phase calculations were performed in a 15 × 15 × 15 Å vacuum unit cell, and the atomic positions were systematically optimized until the maximum force acting on any atom was below 0.05 eV $Å^{-1}$. Gas phase calculations for O_2 were carried out with spin polarization to account for its triplet state. Previous DFT calculations, which studied the electrochemical oxygen revolution and reduction reactions, revealed substantial inaccuracies in the calculated O_2 energies when using the GGA-PBE functional [82,95–98]. To overcome the underestimation of the O_2 gas-phase energy using GGA-PBE functional, a semi-empirical correction of −0.46 eV was incorporated during the calculation.

A two-step optimization procedure, which is more efficient than conventional single-step optimizations, was considered for the geometry relaxation of all the structures. In the initial step, the structures were electronically converged, ensuring that energy differences between iterations were less than 10^{-4} eV, and the maximum force acting on each atom remained below 0.05 eV $Å^{-1}$. Subsequently, in the second step, structures underwent a more rigorous electronic convergence, demanding that energy variations between iterations were less than 10^{-6} eV, while still maintaining the maximum force on each atom below 0.05 eV $Å^{-1}$. The computation of forces for these two steps was facilitated by utilizing a fast Fourier transform grid, with cutoff values set at 1.5 times and 2.0 times the plane-wave cutoff, respectively. A detailed description of the *k*-point selection of bulk geometries, their geometry

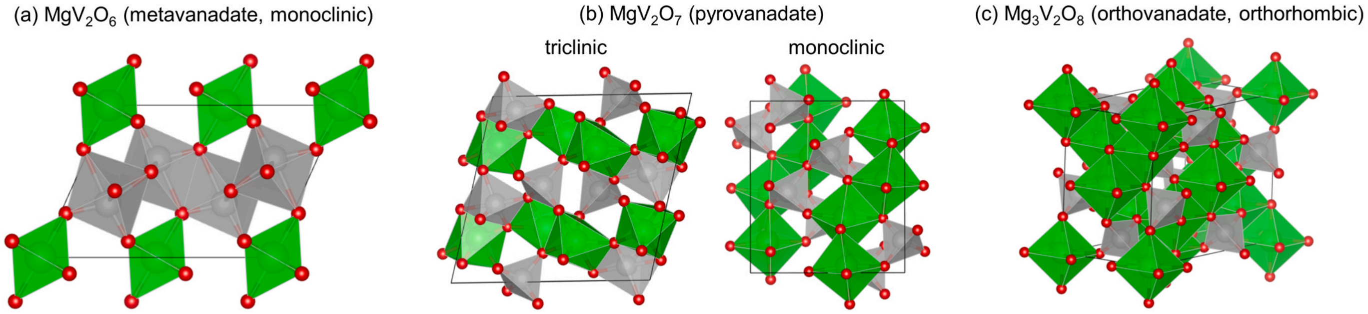

Fig. 1. Bulk structures of MgV_2O_6 (metavanadate, monoclinic), MgV_2O_7 (pyrovanadate, triclinic and monoclinic), and $Mg_3V_2O_8$ (orthovanadate, orthorhombic).

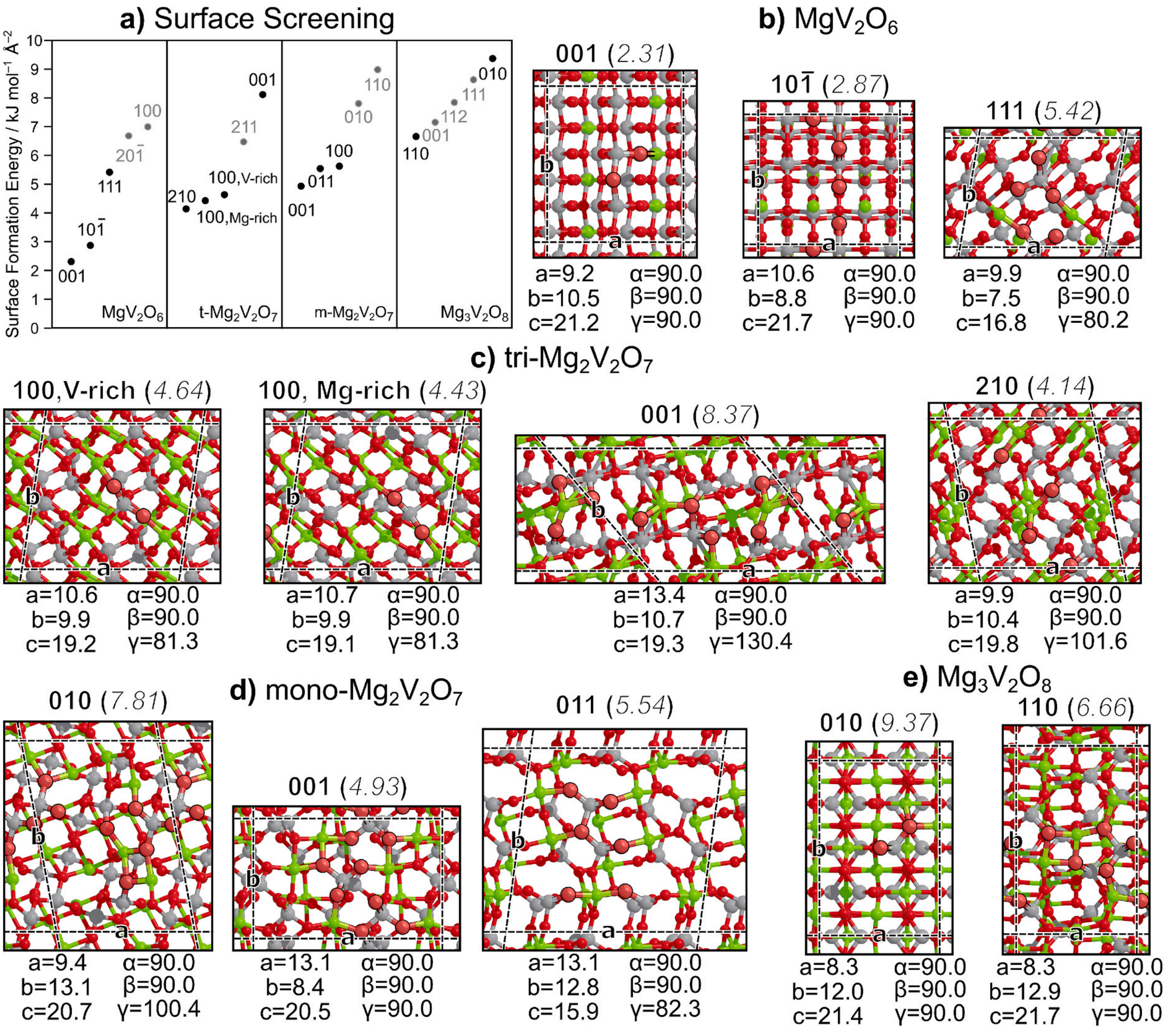

Fig. 2. Mg-vanadates surface screening and slab models. a) Surface formation energy (SFE, kJ mol^{-1} $Å^{-2}$) screening summary (adapted from [51]) for Mg-vanadate surfaces. Slab models for selected surfaces from b) MgV_2O_6, c) tri-$Mg_2V_2O_7$, d) mono-$Mg_2V_2O_7$, and e) $Mg_3V_2O_8$ materials. Miller indexes are provided for each surface, along with its corresponding SFE (kJ mol^{-1} $Å^{-2}$) and optimized cell parameters.

optimization and optimized lattice parameters and angles, and surface formation energy (SFE) calculation of the cleaved surfaces can be found in our previous work.

The exchange energies from swapping a single Mg atom by transition metal dopants on Mg vanadates was investigated for Ni, Cu, and Zn. All surfaces presented in this work correspond to optimized structures upon dopant addition (i.e., we do not assume that the dopant nor the relaxed surface atoms will retain the lattice positions from the undoped counterparts). In addition, doped surfaces were reoptimized from converged adsorbate and transition state structures to test whether local adsorbate-induced reconstructions result in more stable doped surfaces.

Based on the surface formation energy (SFE) analysis reported in our previous work, [51] we examined 12 different Mg-vanadate surfaces (Fig. 2 and Table S1) with 54 undoped surface oxygen reaction sites. Dopants were placed into a variety of near-surface Mg sites (37 unique positions) resulting in a total of 370 O atom-dopant configurations, for each dopant. However, we explicitly explore 324 configurations as we discard a very high-surface formation energy surface (Section 3.1). Transition state searches for C–H activation of C_2H_6 were initiated by employing the nudge elastic band (NEB) method [99–101] with 16 images distributed along the reaction coordinate. After achieving NEB convergence, the transition state structures were identified using the more accurate dimer method [102]. These optimizations continued until the maximum force acting on all atoms in the system dropped below 0.05 eV $Å^{-1}$, following a two-step procedure akin to that outlined for structural optimizations. HAE and MAE energies were calculated by optimizing H* and CH_3* across all O atom-dopant configurations of interest.

3. Results and discussion

3.1. *Surface structure and stability in the presence of dopants*

Here, we explore the role of Ni, Cu, and Zn as substitutional dopants in Mg vanadates with the broader motivation of introducing levers to control and modify catalyst reactivity and selectivity during the ODH of light alkanes. In this work, we examine 12 low-energy Mg-vanadate surfaces (Fig. 2) [51] with varying Mg:V ratios that alter VO_x spacing within the crystal lattice. Across all 12 surfaces, there are a total of 37 crystallographically unique Mg atoms that are allowed to relax in their corresponding slab models, and these were considered as potential surface-dopant locations in this work. To address the relative stability of dopant sites (former Mg lattice positions) on Mg-vanadate surfaces, we calculated the cation exchange energies, according to:

$$\Delta E_{ex} = \left(E_{\text{doped}} + \frac{E_{\text{MgO}}}{n_{\text{Mg}}}\right) - \left(E_{\text{undoped}} + \frac{E_{\text{MO}}}{n_{\text{M}}}\right) \quad (1)$$

where E_{doped} and E_{undoped} are, respectively, the optimized energies of the doped and the undoped slab models, E_{MgO} and E_{MO} are the energies of the cubic MgO bulk and dopant (M) oxide bulk reference (hexagonal NiO, monoclinic CuO, and cubic ZnO), and n_{Mg} and n_{M} correct for stoichiometric differences between slab and bulk models. It is worth noting that these exchange energies reflect the dilute limit of a dopant, as we only exchanged a single Mg atom. For example, the unit cell for the undoped MgV_2O_6 (1 0 0) surface has 12 Mg atoms, 24 V atoms, and 72 O atoms, consistent with the 1:2:6 stoichiometry from the parent bulk structure (MgV_2O_6). However, when exchanging a Mg by a single dopant on MgV_2O_6 (1 0 0), the corresponding stochiometric values for the dopant and Mg would be, respectively $\frac{1}{12} = 0.083$ and $1 - \left(\frac{1}{12}\right) = 0.917$.

Since exchange energies from Equation (1) are biased to the arbitrary selection of the parent metal oxide for both the dopant (E_{MO}) and Mg (E_{MgO}) atoms, these do not necessarily reflect the experimentally relevant stability of dopant sites, therefore, endothermic exchange energies likely would suggest surfaces are metastable and would give little indication as to their real-world stability. In fact, the dopants studied have been observed in metal vanadate structures (Table 1). Moreover, it would be misleading to compare exchange energies across different dopants because of inherent differences among the stabilities of NiO, CuO, and ZnO. Instead, based on the relative energies within a dopant series, we can infer the most likely Mg sites to be exchange within a surface, while qualitatively elucidating the role of Mg atom coordination and environment on exchange energies.

Exchange energies were weakly sensitive to changes in the Mg:V ratio (comparing MgV_2O_6 to $Mg_3V_2O_8$) and changes in SFE (Fig. 3). Ni exchange energies range from −35 to +36 kJ mol^{-1} across 11 of the 12 surfaces, with a slight decrease in exchange energy as Mg:V ratio increases. Ni exchange energies, however, are much lower in the t-$Mg_2V_2O_7$ (0 0 1) surface (more exothermic), ranging from −131 to −33 kJ mol^{-1}. Cu and Zn exhibit a similar behavior, with exchange energies in t-$Mg_2V_2O_7$ (0 0 1) being significantly lower (more exothermic) than the other 11 surfaces. The exothermic exchange energies into t-$Mg_2V_2O_7$ (0 0 1) can likely be explained by its relatively high SFE (8.37 kJ mol^{-1} $Å^{-2}$), which is ~2 × larger than that of the other t-$Mg_2V_2O_7$ surfaces studied here (3.81–4.62 kJ mol^{-1} $Å^{-2}$). Indeed, similar trends (although weaker), can be seen in comparing the surfaces within MgV_2O_6, m-$Mg_2V_2O_7$, and $Mg_3V_2O_8$ bulk materials, (i.e., higher energy surfaces

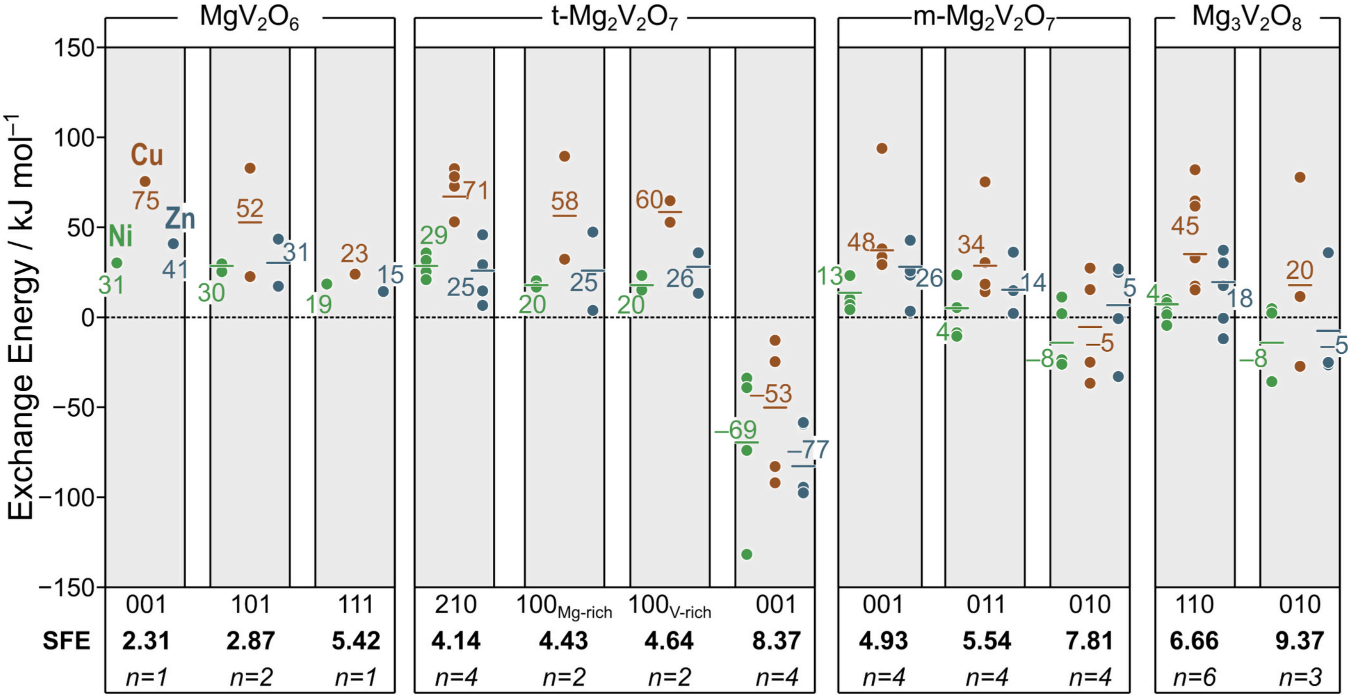

Fig. 3. Exchange energies of Ni (green), Cu (brown), and Zn (blue) doped surfaces for MgV_2O_6, t-$Mg_2V_2O_7$, m-$Mg_2V_2O_7$, and $Mg_3V_2O_8$ classified according to their surface formation energy (SFE, kJ mol^{-1}, **bold**). The average exchange energy of each surface along with the number of unique Mg positions (*n*) is also provided. (For interpretation of the references to colour in this figure legend, the reader is referred to the web version of this article.)

display lower (more exothermic) exchange energies). Overall, data suggests that substitutional doping is more feasible in higher surface formation energy surfaces, which is consistent with the notion that high SFEs reflect an instability of their lattice Mg atoms (making them easier to replace).

Our previous work [51] demonstrated that the lowest SFE facets for V_2O_5 and Mg-vanadate surfaces are those that preserve the V atom coordination from bulk material, so that there are no undercoordinated V atoms across the presented surfaces herein. The preservation of V coordination upon surface cleavage, however, occurs at the expense of breaking the coordination of Mg atoms from that of the bulk material, so that SFE values inherently reflect the relative stability of these undercoordinated Mg sites. As such, we classified the unique 37 exchange locations (Mg-atoms) by their local coordination (Fig. 4). Indeed, exchange energies become more endothermic with increasing exchange site coordination number. This suggests that undercoordinated Mg are easier to exchange with substitutional dopants than higher coordinated counterparts. For example, the average exchange energies for Cu into m-$Mg_2V_2O_7$ ranges from −37 into MgO_3 sites to +93 into MgO_6 sites, with similar trends observed for other dopants across all catalyst compositions. Generally, undercoordinated Mg atoms mostly occupy lattice positions near the surface, and thus their more favorable exchange energies (Fig. 4) suggest that Ni, Cu, and Zn will likely be exposed on the surface (i.e., not entrapped within the bulk), which is desired for exploiting dopants influence during ODH catalysis.

The most stable exchange site for a given surface is the same regardless of substitutional dopant. In fact, exchange energies of Cu, Zn, and Ni all correlate with one another (Fig. S1). This further suggests that exchange energies are driven by the stability of the Mg-atom in the undoped lattices, rather than by stabilities of the dopant atoms (which might vary). These 12 structures, highlighting the most stable M–to–Mg (M: Zn, Cu, Ni) exchange sites are shown for Cu in Fig. 5. While most of the dopant atoms in the doped surfaces retained the former lattice location of the Mg atom, some of the surfaces undergo restructuring. For example, the Cu locations in MgV_2O_6 (111) and $Mg_3V_2O_8$ (010) surfaces are significantly different than that of the former Mg (exchange site, Fig. S2). Both the MgV_2O_6 (111) and the $Mg_3V_2O_8$ (010) are among the highest surface formation energy surfaces presented herein, and accordingly, they result in more restructuring after the addition of the dopant transition metal. Of course, given their high SFE values, they are less likely to be present in polycrystalline materials (and thus less relevant for chemistry) than the other surfaces studied here.

3.2. *Impact of dopants on surface reducibility*

Oxygen vacancy formation energy (VFE) and hydrogen addition energy (HAE) calculations are typically explored as reduction proxies on metal oxide catalysts. In our previous work, VFE was found to be a relatively poor predictor of C_1–C_3 alkane activation energies on V_2O_5 and $Mg_xV_2O_{5+x}$ catalyst surfaces, while HAE was adequate but exhibited some scattering because of strong H-bonding (present in H*, but not on transition state structures) [51]. HAE has been previously shown to correlate with C–H bond activation energies in alkanes and alkanols on a range of oxide catalysts, such as CeO_2, [103] NiO, [64] MoVTeNbO (001), [62] $BiVO_4$, [104] Co_3O_4, [63] and polyoxometalates [4]. We recently reported that, while HAE is adequate in describing C–H activation of light alkanes on V_2O_5 and Mg-vanadates surfaces, methyl-addition energies (MAE, a CH_3* probe) outperforms HAE because they avoid the misleading H-bonding interactions mentioned above [51]. As such, we extended our previous calculations and explored HAE and MAE for all 54 unique surface O atoms with Ni, Cu, and Zn dopants in each of the 37 Mg sites examined (Section 3.1). While there are only 37 distinct exchange locations in bare undoped surfaces, the addition of an adsorbate (H* and CH_3*) breaks the otherwise symmetrical Mg locations. This, in turn, effectively introduces a larger configurational space of dopant-adsorbate locations within each surface (370 total, per dopant, per adsorbate).

In this work, we calculate HAE values as the reaction energy for:

$$MO + \frac{1}{2}H_2O_{(g)} \rightarrow MO\text{-}H + \frac{1}{4}O_{2_{(g)}} \quad (2)$$

where gaseous O_2 and H_2O are used here to balance the H addition rather than alternatives such as a H radical or ½ H_2 that are not present during ODH reactions. This reaction thus is a better proxy to the thermodynamics present during ODH and thus informs about the thermodynamic tendency of a reaction site to be hydroxylated if it were in equilibrium with gas-phase O_2 and H_2O. Nevertheless, the trends presented herein would remain consistent regardless of choice of balancing gas phase species. MAE values are calculated as the reaction energy for:

$$MO + \frac{1}{4}O_2 + CH_4 \rightarrow MO\text{-}CH_3 + \frac{1}{2}H_2O \quad (3)$$

where, similar to equation (2), we chose a combination of CH_4, O_2, and H_2O as the gas-phase reference rather than methyl radicals.

The t-$Mg_2V_2O_7$ (001) surface exhibited very large SFE values and dopant exchange energies that were significantly more exothermic than the other 11 surfaces examined in this work (Fig. 3). These large exothermic dopant exchange energies, furthermore, accompanied large restructuring of the surface, underlying the instability of the undoped (or doped) surface, and thus it was excluded from further analysis.

HAE values on undoped Mg vanadate surfaces range from 17 to 221

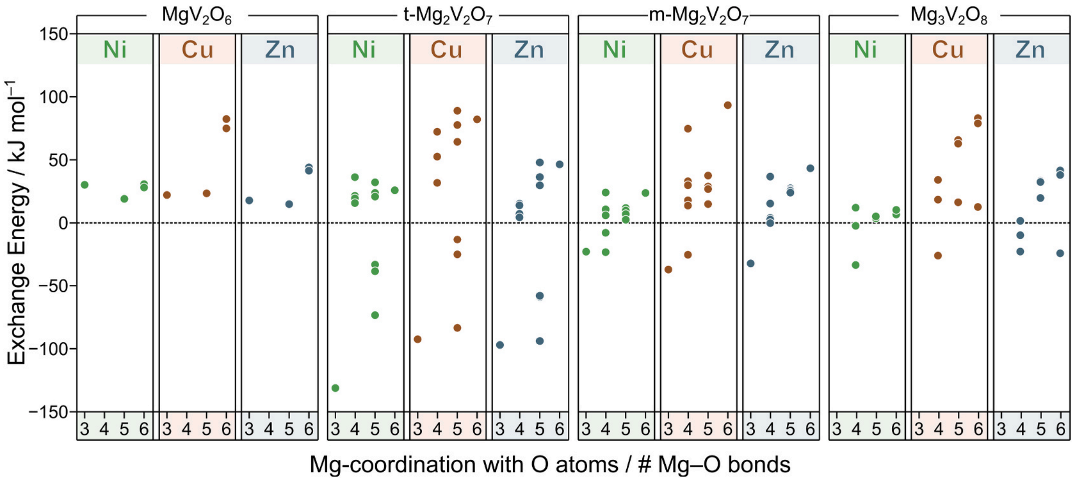

Fig. 4. Exchange energies for Ni, Cu, and Zn-doped (a) MgV_2O_6, (b) t-$Mg_2V_2O_7$, (c) m-$Mg_2V_2O_7$, and (d) $Mg_3V_2O_8$ surfaces as a function of Mg coordination with O.

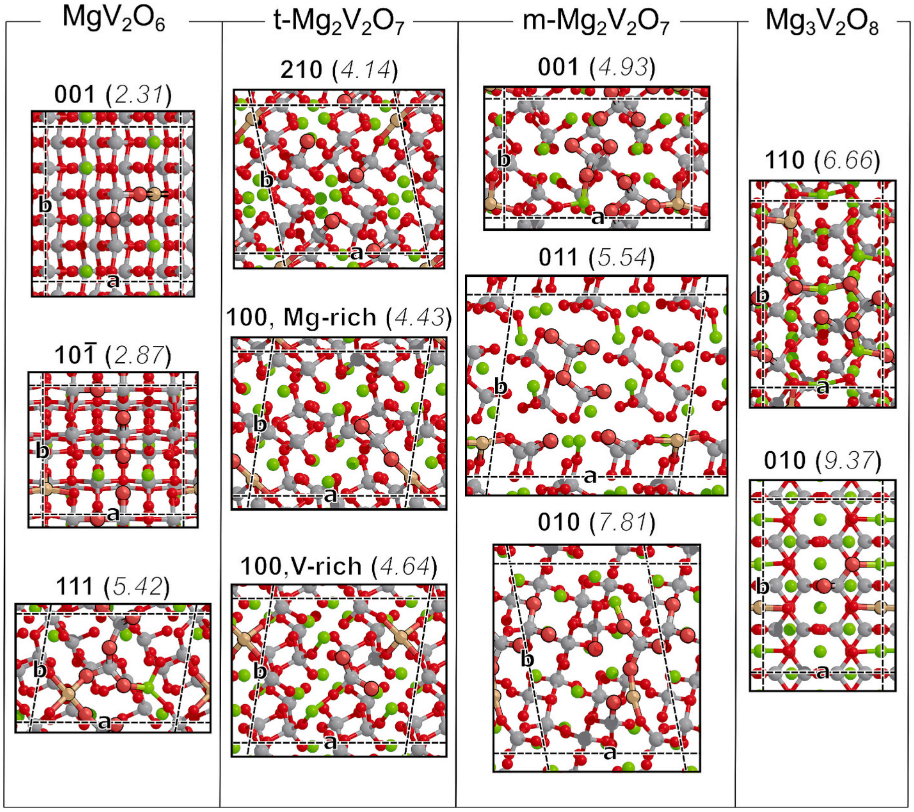

Fig. 5. Cu-doped (a) MgV_2O_6, (b) t-$Mg_2V_2O_7$, (c) m-$Mg_2V_2O_7$, and (d) $Mg_3V_2O_8$. Cu is shown in the most favorable exchange site for each surface. Surface formation energies (absent any dopant) are shown in parentheses for each surface. The gray, red, green, and tan colored atoms denote the V, O, Mg, and Cu, respectively. (For interpretation of the references to colour in this figure legend, the reader is referred to the web version of this article.)

kJ mol^{-1} across the 54 surface O atoms present in their corresponding lattices. These endothermic values (referenced to gas-phase H_2O and O_2) suggest that hydroxyl (O–H) coverage is likely to be low at reasonable reaction conditions, as discussed further in our previous work [51]. Generally, increasing Mg:V content leads to increases in HAE values, as suggested by averages across bulk materials of 68 kJ mol^{-1} for MgV_2O_6, 79 kJ mol^{-1} for t-$Mg_2V_2O_7$, 111 kJ mol^{-1} for m-$Mg_2V_2O_7$, and 122 kJ mol^{-1} for $Mg_3V_2O_8$ undoped surfaces [51]. The corresponding averages for HAE values in Ni-doped surfaces were calculated to be, respectively, 72, 87, 110, and 103 kJ mol^{-1} for MgV_2O_6, t-$Mg_2V_2O_7$, m-$Mg_2V_2O_7$, and $Mg_3V_2O_8$. For the case of Cu, average HAE values were found to be, respectively, 46, 49, 82, and 43 kJ mol^{-1} for MgV_2O_6, t-$Mg_2V_2O_7$, m-$Mg_2V_2O_7$, and $Mg_3V_2O_8$. Lastly, the corresponding average HAE values in Zn-doped surfaces were calculated to be, respectively, 72, 88, 111, and 125 kJ mol^{-1} for MgV_2O_6, t-$Mg_2V_2O_7$, m-$Mg_2V_2O_7$, and $Mg_3V_2O_8$.

While the average HAE values remain endothermic, Cu-doped surfaces exhibit the lowest average HAE values (relative to undoped surfaces, Fig. 6), followed by Ni and Zn. Higher SFE surfaces have more-exothermic HAE values and the extent is more significant with the presence of Cu dopant compared to that of Ni and Zn. While the lower HAE values per each structure correspond to low and intermediate Mg-contents on undoped catalysts (being generally lower for MgV_2O_6 and m-$Mg_2V_2O_7$ surface), the corresponding HAE values on doped surfaces are more exothermic in t-$Mg_2V_2O_7$ and $Mg_3V_2O_8$, especially in the

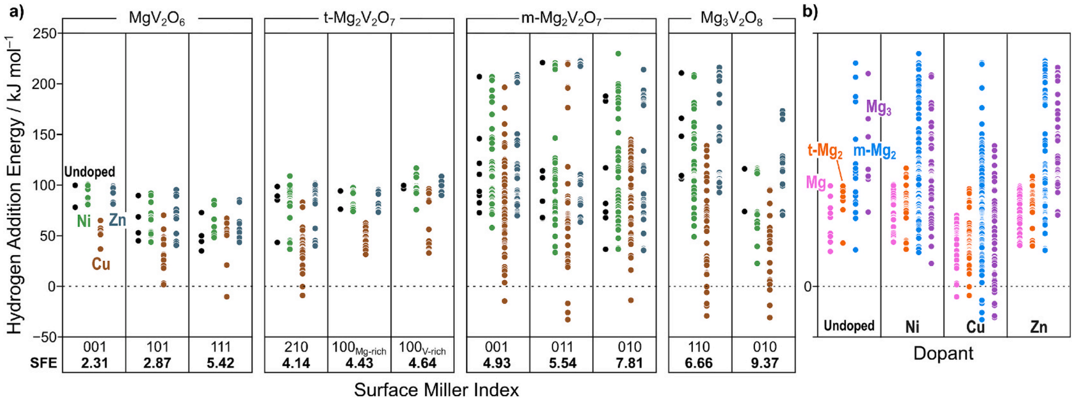

Fig. 6. Hydrogen addition energies (HAE) on Mg-vanadate surfaces: (a) undoped (black), Ni-doped (green), Cu-doped (brown), and Zn-doped (grey blue) on MgV_2O_6, t-MgV_2O_7, m-$Mg_2V_2O_7$, and $Mg_3V_2O_8$ surfaces. The Miller index for each surface is provided along with the surface formation energy (SFE) of the undoped surface. (b) Same data as in part (a), organized by dopant and colored based on the surface: MgV_2O_6 (pink), t-MgV_2O_7 (orange), m-$Mg_2V_2O_7$ (light blue), and $Mg_3V_2O_8$ (purple). (For interpretation of the references to colour in this figure legend, the reader is referred to the web version of this article.)

presence of Cu dopant. This, in turn, suggest that dopants moderate the reducibility of undoped lattice O atoms by making the most reducible sites on undoped materials less reducible while making the least reducible sites on undoped surfaces more reducible. These observations are consistent with MAE values (Fig. S3, SI) and can have important implications in tuning electronic properties to enhance catalyst reactivity while not compromising the desired selectivity that is likely mostly governed by geometric isolations of VO_x.

The role of substitutional doping was quantified calculating shifts in HAE and MAE values by contrasting those for doped surfaces relative to their undoped counterparts as:

$$\mathrm{HAE_{shift}} = \mathrm{HAE_{doped}} - \mathrm{HAE_{undoped}} \tag{4}$$

$$\mathrm{MAE_{shift}} = \mathrm{MAE_{doped}} - \mathrm{MAE_{undoped}} \tag{5}$$

These $\mathrm{HAE_{shift}}$ and $\mathrm{MAE_{shift}}$ values (Fig. 7) reflect how H* (or CH_3*) adsorption to a specific O atom is influenced by the presence of a nearby dopant (i.e., exothermic shifts indicate that the reaction site became more reducible). $\mathrm{HAE_{shift}}$ and $\mathrm{MAE_{shift}}$ values still show significant spread within a given surface, likely because differences in the configurational space of dopant-adsorbate combinations, (e.g., varying distances between dopant and O-atoms within these data sets). $\mathrm{HAE_{shift}}$ values on doped surfaces range from -116 kJ $\mathrm{mol^{-1}}$ to $+59$ kJ $\mathrm{mol^{-1}}$ with Ni, from -194 to $+39$ kJ $\mathrm{mol^{-1}}$ with Cu, and from -73 to $+58$ kJ $\mathrm{mol^{-1}}$ with Zn. Despite the large spreads, Ni and Zn dopants induce, on average, slight changes to HAE (–1.9 and 2.3 kJ $\mathrm{mol^{-1}}$, respectively) and MAE (–4.0 and 1.5 kJ $\mathrm{mol^{-1}}$ respectively). Cu, in contrast, lowers HAE and MAE values, respectively, by averages of –39.0 and –41.1 kJ $\mathrm{mol^{-1}}$. Comparing $\mathrm{HAE_{shift}}$ values across different structures, shifts are generally more exothermic at high Mg:V ratios (i.e., in $Mg_3V_2O_8$), and similar trends are present in $\mathrm{MAE_{shift}}$ values. These shifts, on average, are weakly influenced, if at all, by SFE values.

Overall, Cu has the largest impact on surface reducibility. Cu can reduce HAE (and MAE) values by as much as -194 kJ $\mathrm{mol^{-1}}$ (-208 kJ $\mathrm{mol^{-1}}$ for MAE) or increase them by as much as 39 kJ $\mathrm{mol^{-1}}$ (22 kJ $\mathrm{mol^{-1}}$ for MAE). Furthermore, the average $\mathrm{HAE_{shift}}$ and $\mathrm{MAE_{shift}}$ values for Cu are larger (in magnitude) than those of Ni and Zn. This is likely because single reduction of Cu is easiest than that of Ni and Zn, as described further in Section 3.3. These shifts in reducibility are expected to tune the reactivity of the surface for alkane activation, as discussed further in Section 3.4 below.

3.3. Features impacting the role of dopants

Here, we rationalize the observed $\mathrm{HAE_{shift}}$ and $\mathrm{MAE_{shift}}$ values (Section 3.2) to determine what features of the surface, namely the exchange site, reaction site, or dopant identity may allow one to predict whether the dopant will increase or reduce the reactivity of nearby O atoms within the surface lattice.

The significant scatter between exchange energies and $\mathrm{HAE_{shift}}$ and $\mathrm{MAE_{shift}}$ values (Fig. 8) suggest that exchange energies do not solely govern the extent at which a dopant influences H* and CH_3* adsorption relative to that on the undoped surfaces. This makes sense, as some reactive sites were modified further from dopant sites than others, so a range of $\mathrm{HAE_{shift}}$ values is expected for a given dopant exchange site. Consistent with Fig. 7, these data (Fig. 8) suggest that Cu induces the largest $\mathrm{HAE_{shift}}$ and $\mathrm{MAE_{shift}}$ values, in both easy-to-exchange and hard-to-exchange sites. Overall, there is little observable correlation between $\mathrm{HAE_{shift}}$ (or $\mathrm{MAE_{shift}}$) values and the exchange energies.

Our previous work showed that, in general, atop and bridged O-atoms are more reactive than 3-fold counterparts on V_2O_5 and Mg-vanadate surfaces. $\mathrm{HAE_{shift}}$ and $\mathrm{MAE_{shift}}$ values, however, do not generally correlate with the O atom coordination (Fig. S4, SI). This suggest that shifts in HAE and MAE values are not governed by O atom coordination. However, there is a negative trend between $\mathrm{HAE_{shift}}$ values and the HAE (Fig. 9) of the same O atom in the undoped surface (with a similar trend seen for MAE, Fig. S5, SI). $\mathrm{HAE_{shift}}$ values are more exothermic for O atoms that have a more endothermic HAE in the undoped surface. In other words, dopants often make more-reducible O atoms (in the undoped surface) less reducible in the doped surface and make less-reducible O atoms more reducible in the doped surface. This suggests that dopants may have a moderating impact on surface reducibility, and since these HAE and MAE values correlate with alkane activation barriers, dopants may also moderate average alkane barriers across a given surface. However, while these trends can give insights into the underlying chemistry of these surfaces, the most reactive oxygen (for a given surface and dopant position) is likely to dominate the observed chemistry, such that the most-reactive O sites take on a greater significance than the surfaces' average reactivity.

We further examined whether any correlation was present between the O atom (reaction site) and the dopant distance and their corresponding shifts in reducibility ($\mathrm{HAE_{shift}}$ and $\mathrm{MAE_{shift}}$). Large dopant-O distances ($>$ 5 Å, Fig. S6) generally had weaker impacts on HAE or MAE ($\mathrm{HAE_{shift}}$ and $\mathrm{MAE_{shift}}$ values closer to 0), but no significant trend is

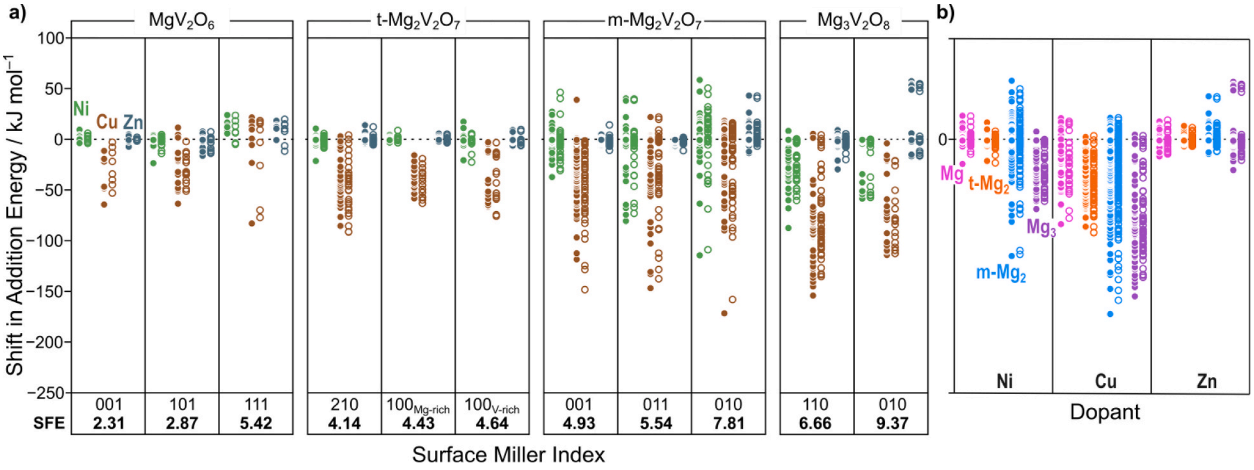

Fig. 7. Shift in hydrogen and methyl addition energies on Mg-vanadate surfaces: (a) $\mathrm{HAE_{shift}}$ (filled) and $\mathrm{MAE_{shift}}$ (hollow) on Ni-doped (green), Cu-doped (brown), and Zn-doped (grey blue) MgV_2O_6, t-MgV_2O_7, m-$Mg_2V_2O_7$, and $Mg_3V_2O_8$ surfaces. The Miller index for each surface is provided along with the surface formation energy (SFE) of the undoped surface. (b) Same data as in part (a), organized by dopant and colored based on the surface: MgV_2O_6 (pink), t-MgV_2O_7 (orange), m-$Mg_2V_2O_7$ (light blue), and $Mg_3V_2O_8$ (purple). (For interpretation of the references to colour in this figure legend, the reader is referred to the web version of this article.)

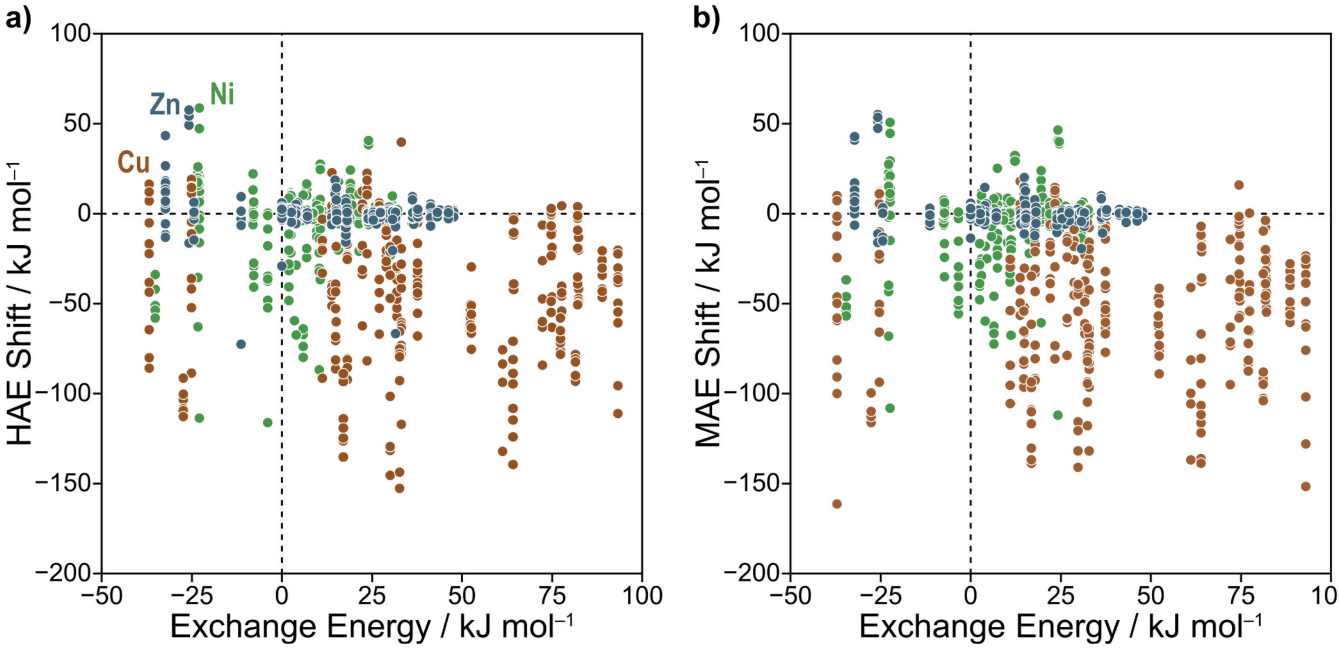

Fig. 8. The exchange energy of Ni (green), Cu (brown), and Zn (grey blue) doped surfaces as a function of (a) shift in hydrogen addition energy (HAE) and (b) methyl addition energy (MAE) across all doped Mg-vanadate surfaces examined in this work (MgV_2O_6, t-$Mg_2V_2O_7$, m-$Mg_2V_2O_7$and $Mg_3V_2O_8$ surfaces). (For interpretation of the references to colour in this figure legend, the reader is referred to the web version of this article.)

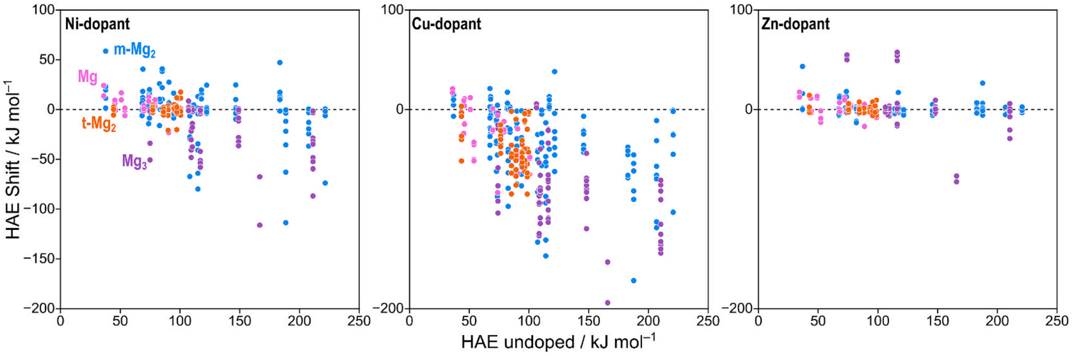

Fig. 9. Shift in HAE values upon doping as a function of the HAE of undoped surfaces for a) Ni-, b) Cu- and c) Zn-doped MgV_2O_6 (pink), t-$Mg_2V_2O_7$ (orange), m-$Mg_2V_2O_7$ (blue), and $Mg_3V_2O_8$ (purple). Fig. S6 in the SI shows corresponding data for MAE. (For interpretation of the references to colour in this figure legend, the reader is referred to the web version of this article.)

observed for those within <5 Å. These shifts are also shown to not correlate with the degree to which surfaces restructure between the undoped and the doped surfaces (Fig. S7). Overall, these data suggest that geometric probes are not adequate to describe the observed HAE_{shift} and MAE_{shift} values.

We also analyzed whether the dopant or a nearby V atom was reduced upon H* or CH_3* adsorption. As stated above, substitutional doping by Ni, Cu, and Zn introduces a new potential reduction center by replacing an otherwise non-reducible lattice Mg atom. Among the studied dopants, only Cu has a reported standard reduction potential for a 2+ to 1+ transition, [75] suggesting that it is more likely to adopt a 1+ state than either Ni or Zn. Similarly, while Cu_2O is a known oxide, neither Ni_2O nor Zn_2O have been reported. Comparing their two-electron potentials (2+ to 0), the standard electrode potentials range as +0.34> −0.23> −0.76 eV for Cu, Ni, and Zn, respectively, [75] consistent with Cu being most prone towards reduction.

To determine the oxidation states of reduced doped $Mg_xV_2O_{5+x}$ surfaces, we examined the population analysis on the V atoms reported in DFT+U calculations. The DFT+U method reports population matrices describing orbital occupancies for each element on which the DFT+U model was used (here, for V cations). These matrices were used to obtain the formal oxidation state of lattice V-atoms. If the V was not reduced from V^{5+} to V^{4+} by H* or CH_3* adsorption, we assumed that the reduction occurred on the dopant atom instead.

On Zn-doped surfaces, H* and CH_3* reduced the Zn dopant in only 8 % of the structures. Ni was more frequently reduced (26 %), and Cu was the most frequently reduced (82 %). Notably, the reduced atom (either V or the dopant) was the same for H* and CH_3* structures. It is worth noting that the identity of the reduction center (V or dopant) is sensitive to whether U corrections are applied to dopant atoms. For example, the oxidation states on V- and Mn-doped CeO_2 (1 1 1) surfaces upon vacancy formation were found to be dependent on whether a U correction was applied to V and Mn dopants [70]. However, in the present work, we explored 360 configurations for H*, CH3*, and C–H activation barriers for each dopant and our methods do not preferentially reproduce the same reduction center across our calculations. Instead, only in a fraction of Ni-, Cu-, and Zn-doped surfaces (26 %, 82 %, and 8 %, respectively) the dopant was reduced. The greater fraction of Cu-reductions, compared to Ni and Zn, follows their expected reducibilities.

As expected, when dopants are reduced, there are larger (and generally exothermic) shifts in HAE and MAE values (Fig. 10). For example, when Cu is reduced to Cu^{1+}, the average HAE_{shift} is −51 kJ mol^{-1}, while the HAE_{shift} is +5 kJ mol^{-1} for Cu-doped surfaces where the V is reduced (to V^{4+}) instead. The impact of reducibility is also shown for Ni to a lesser extent than that for Cu (HAE_{shift} averages go from +2 kJ mol^{-1} when V is reduced to −24 kJ mol^{-1} when Ni is reduced), and basically no change in HAE (or MAE) is observed in the few instances where Zn is reduced. Given the challenge of placing Zn into a 1+ oxidation state, and the indirect method we are following for observing these reductions, we find it unlikely that those results correspond to Zn reduction and are actually just artifacts in the population analysis we are performing.

3.4. *Initial C–H activation of C_2H_6 on doped Mg-vanadate surfaces*

Our previous work explored the initial C–H activation of C_1–C_3 alkanes and established that (1) increasing Mg:V ratios leads to higher alkane activation barriers (when considering the most likely reaction sites for V_2O_5 and each Mg vanadate catalyst), (2) atop or bridging O atoms are the reaction sites on all surfaces, being more reactive than their 3-fold counterparts, and (3) HAE and MAE values strongly correlate with alkane activation barriers.

Here, we study the initial C–H activation of C_2H_6 on Ni-, Cu-, and Zn-doped Mg vanadate catalysts to explore if the changes in O-atom reducibility (HAE and MAE values) described above will impact alkane reactivity. Initial C–H activation barriers for C_2H_6 on all Mg-vanadate surfaces (except for t-$Mg_2V_2O_7$ (001)) with the presence of Ni, Cu, and Zn dopants along with their undoped surfaces are shown in Fig. 11. When considering the lowest barrier per surface, we find that Cu-doped surfaces are always more reactive than their undoped counterparts. This is also true for most, but not all, Ni- and Zn-doped surfaces. Organized by surface formation energy, there is significant scatter in the data as we are considering all symmetrically unique reactive O sites and all near-surface Mg sites.

Similar to Equations (4)–(5), we also calculated the shift in C–H activation barriers caused by the substitutional dopant as:

$$E_{act,shift} = E_{act,doped} - E_{act,undoped} \tag{6}$$

where the $E_{act,doped}$ and $E_{act,undoped}$ are, respectively, the C–H activation barrier on doped and undoped surfaces. Similar to HAE and MAE shifts, the corresponding shifts in C–H activation between doped and undoped surfaces are occurring on the same surface O atom, thus allowing to directly address on the impact of the dopant rather than other factors that influence reaction, such as O-atom coordination and environment. These shifts in C–H activation barriers (Fig. 12) are generally exothermic, suggesting C–H bond cleavage is energetically more favorable on doped surfaces, particularly on Cu-doped surfaces. For example, the average $E_{act,shift}$ values on Cu-doped surfaces are –47, –70, –111, and –131 kJ mol^{-1} for MgV_2O_6, t-$Mg_2V_2O_7$, m-$Mg_2V_2O_7$, and $Mg_3V_2O_8$. These average values are all exothermic, suggesting that Mg vanadates, irrespective of composition, become more reactive upon doping. This is also observed across average $E_{act,shift}$ values on Ni-doped (–20, –18, –84, and –88 kJ mol^{-1}) and Zn-doped (–20, –18, –84, and –88 kJ mol^{-1}) MgV_2O_6, t-$Mg_2V_2O_7$, m-$Mg_2V_2O_7$, and $Mg_3V_2O_8$ surfaces. In addition, average $E_{act,shift}$ values across all dopants becomes more exothermic with increasing Mg:V ratios, suggesting that surfaces with higher Mg content benefit the most upon doping.

Alkane C–H activation on V_2O_5 and undoped Mg vanadate surfaces generally occurs with higher barriers as the Mg content increases, as the lowest alkane activation energies increases from 118 kJ mol^{-1} on V_2O_5 to 163 kJ mol^{-1} on $Mg_3V_2O_8$, discussed in more detail in our previous work [51]. Among the 11 Mg-vanadate surfaces studied here, we examined alkane activation into Cu-doped surfaces involving 33 different Cu-exchange sites (Mg positions) in the surface. In nearly all exchange sites (30 of 33), ethane activation occurs with a lower barrier on the Cu-doped surface than on the undoped surface (Fig. 13). These changes in the ethane activation energies on these surfaces range from −176 to +61 kJ mol^{-1}, with an average decrease of −37 kJ mol^{-1} across all surfaces. While this is consistent with shifts in electronic barriers (per O-atom) being generally exothermic for Cu (Fig. 12), barrier-shifts per O can be misleading because some barrier-shifts correspond to O atoms that may not be reactive during catalysis.

The large impact that Cu can have on the reducibility of doped Mg vanadates is shown when focusing on the lowest-energy barriers for each surface (Fig. 13), irrespective of reactive site (i.e., O atom). For one surface (m-$Mg_2V_2O_7$ (010)), the location of the Cu dopant is critical, as one of the exchange sites lowers the barrier by ~30 kJ mol^{-1}, while two others raise it by 20–30 kJ mol^{-1}, and the fourth site has essentially no impact on the barrier. For the 10 other surfaces, however, the Cu dopant lowers the barrier regardless of the exchange site. While the data across many surfaces enables establishing overall trends on reactivity, we emphasize that the results on the lowest energy surfaces (MgV_2O_6 (001), t-$Mg_2V_2O_7$ (210), m-$Mg_2V_2O_7$ (001), and $Mg_3V_2O_8$ (1 1 0)) are likely the most relevant for catalysis, as those surfaces are expected to make up the

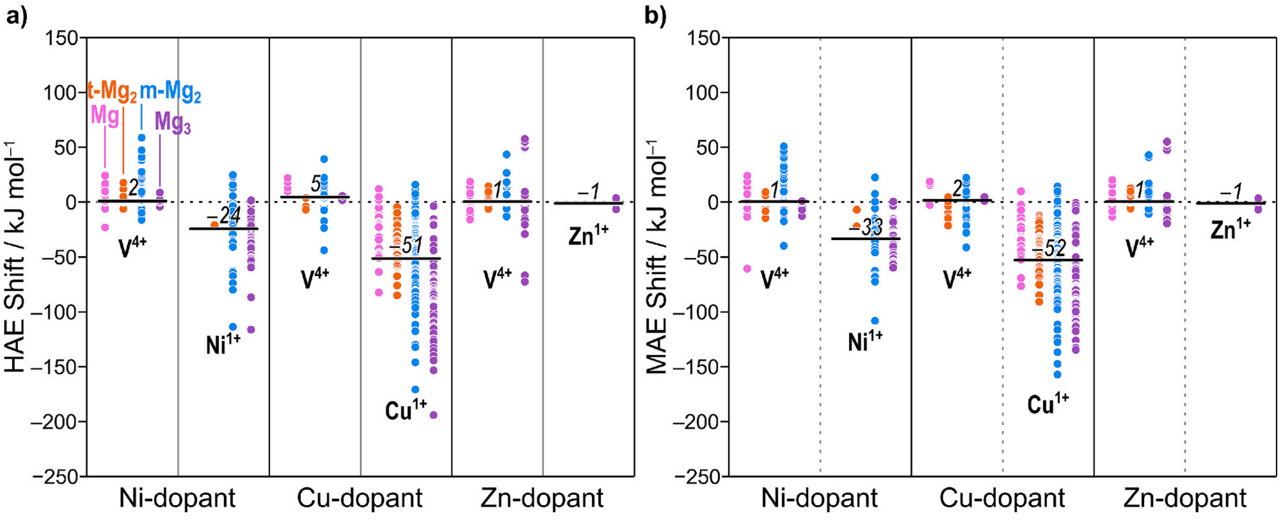

Fig. 10. (a) HAE and (b) MAE shifts as a function of oxidation state of the V atom as well as the substitutional dopant during the addition of $^{*}H$ and $^{*}CH_3$ on the O atom of the Mg-vanadate catalyst surfaces. Oxidation states of Ni, Cu, and Zn are inferred from the V oxidation states from the population analysis given by DFT-U methods, thus, the two instances with Zn^{1+} states may be artifacts of this population analysis, rather than true reductions.

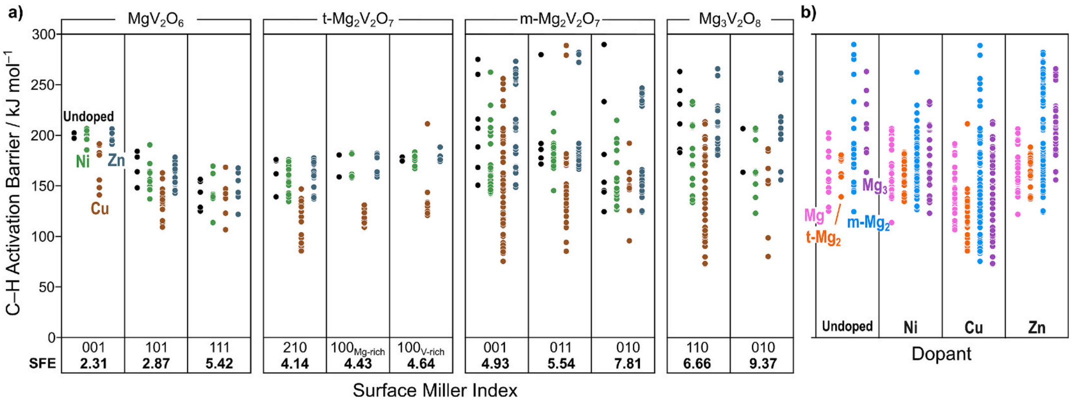

Fig. 11. (a) Electronic energy barriers for the C–H bond activation in ethane (C_2H_6) on undoped (black), Ni- (blue), Cu- (red), and Zn-doped (green) Mg-vanadate surfaces. (b) Electronic barriers for C–H activation in C_2H_6 on MgV_2O_6 (pink), t-$Mg_2V_2O_7$ (orange), m-$Mg_2V_2O_7$ (blue), and $Mg_3V_2O_8$ (purple) surfaces. Surface formation energies (SFE, kJ mol^{-1}) along their corresponding Miller index are also provided. (For interpretation of the references to colour in this figure legend, the reader is referred to the web version of this article.)

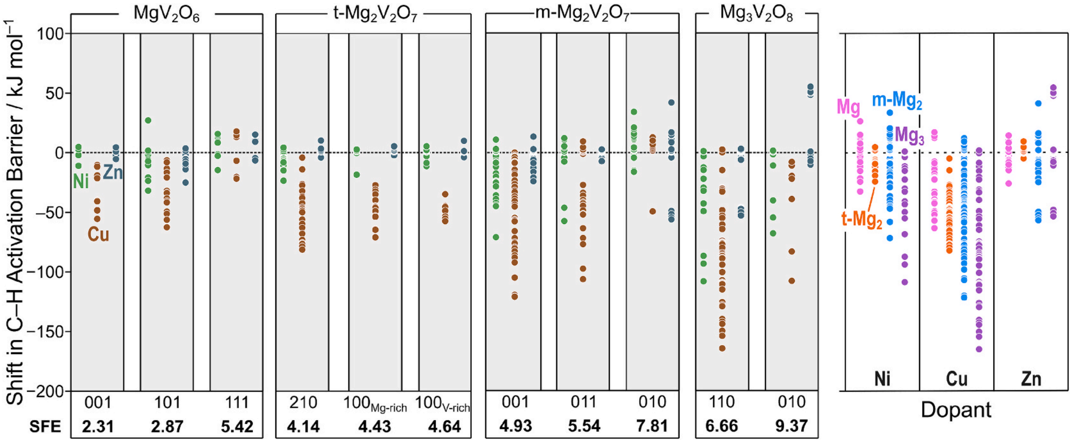

Fig. 12. (a) Shift in electronic energy barriers for the C–H bond activation in ethane (C_2H_6) on undoped (black), Ni- (blue), Cu- (red), and Zn-doped (green) Mg-vanadate surfaces. (b) Shift in electronic barriers for C–H activation in C_2H_6 on MgV_2O_6 (pink), t-$Mg_2V_2O_7$ (orange), m-$Mg_2V_2O_7$ (blue), and $Mg_3V_2O_8$ (purple) surfaces. Surface formation energies (SFE, kJ mol^{-1}) along their corresponding Miller index are also provided. (For interpretation of the references to colour in this figure legend, the reader is referred to the web version of this article.)

majority of polycrystalline Mg-vanadate catalysts. The corresponding data on Ni- and Zn-doped surfaces suggest that these dopants do not increase the overall reactivity of Mg-vanadates, except for 5 out of 9 exchange sites on Ni-doped $Mg_3V_2O_8$ surfaces, further demonstrating that less reactive surfaces (increasing Mg:V ratios) benefit the most upon doping.

While Ni makes less reducible O atoms more reactive (Fig. 12), it does not increase the reactivity relative to the best undoped counterpart (Fig. 13). Instead, Ni-doped surfaces would exhibit the same overall reactivity as undoped surfaces, because the increased reactivity of less reducible O atoms is evened by the decreased or unchanged reactivities of reducible O atoms. Cu, in contrast, induces exothermic shifts that outperform the best barriers from undoped surfaces, and thus Cu-doped surfaces would be expected to be more reactive, likely as a result of increasing the reactivity of former unreactive lattice O-atoms. In fact, only 42 % of the best C–H activation transition states on Cu-doped surfaces occur at the same O atom from the undoped counterpart. This number increases for Ni-doped (76 %) surfaces, followed by Zn (91 %) for which almost all transition states occur at the same O-atom from the undoped counterpart. These percentages trend with the extent of exothermic shifts in HAE, MAE, and C–H activation barriers, further suggesting that dopants modify the reactivity of Mg-vanadates by increasing the reducibility of former unreactive O atoms (which is, in turn, a result of introducing new reduction centers), rather than reinforcing the reducibility of most reactive O atoms in undoped surfaces.

Alkane activations have been shown to correlate with HAE and MAE values of the O sites being reduced, including on doped surfaces. For example, HAE values on transition-metal doped Co_3O_4 were used to screen dopants prior to alkane transition state searches, [63] and this study also showed that the correlation of HAE with alkane activation barriers was consistent and transferrable across materials with different dopants. In our previous work examining V_2O_5 and undoped Mg vanadates, however, MAE outperforms HAE because some surface-bound H* undergo H-bonding with nearby surface O atoms, such that they do not resemble the H orientation in transition state structures. Here, we show correlations between alkane activation barriers and HAE (Fig. 14a) and MAE (Fig. 14b) for all three dopants. As before, we see correlations with MAE result in less scatter than those with HAE, also because of spurious H-bonding that can influence HAE energies. The correlation is best for undoped materials, followed by Zn, Cu, and Ni, according to the R^2 fitness metrics. There is also variation in the slopes of these correlations and y-intercepts, but these variations are unlikely to be statistically significant. Overall, the correlations in Fig. 14b suggest that the same governing physics relating MAE to alkane activation energies applies to doped and undoped surfaces alike, discussed in more detail in our previous work [51].

While this work does not explicitly address how dopants may modify

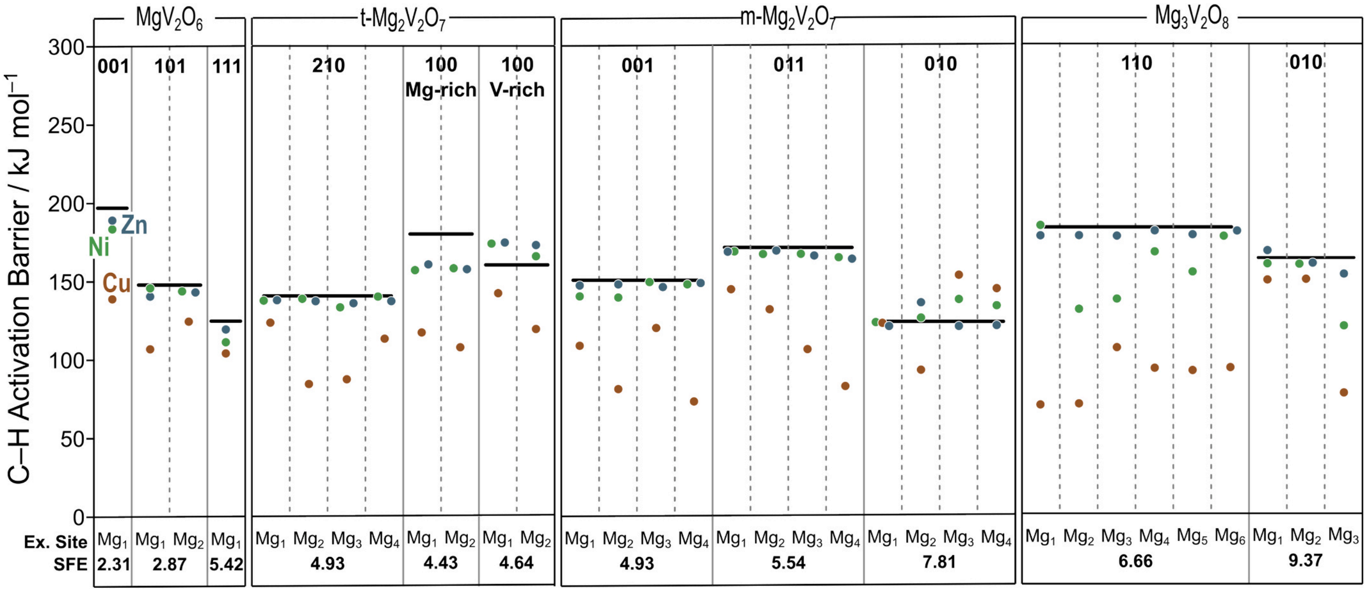

Fig. 13. Lowest C–H activation barriers for ethane (C_2H_6) on Ni-(green), Cu- (brown) and Zn-doped (blue) MgV_2O_6, t-$Mg_2V_2O_7$, m-$Mg_2V_2O_7$, and $Mg_3V_2O_8$ surfaces. Black lines indicate the corresponding lowest barrier from the undoped counterparts. Data is organized by surface formation energies (labeled near the x-axis in **bold**) and presented for each unique Mg exchange site (33 total) within each surface. (For interpretation of the references to colour in this figure legend, the reader is referred to the web version of this article.)

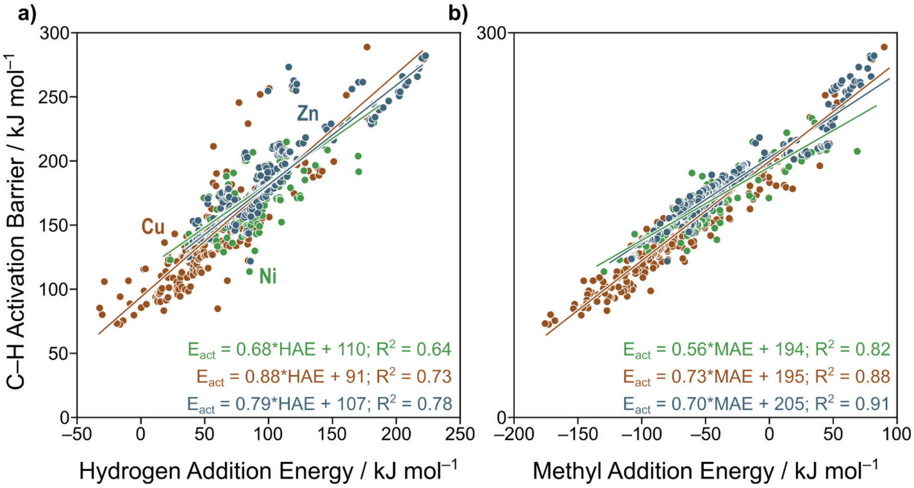

Fig. 14. Electronic C–H activation barrier for ethane (C_2H_6) as a function of the (a) hydrogen addition energy (HAE) and (b) methyl addition energy (MAE) on Ni-(green), Cu- (brown), and Zn-doped (blue) MgV_2O_6, t-$Mg_2V_2O_7$, m-$Mg_2V_2O_7$, and $Mg_3V_2O_8$ surfaces. Each data point in (a) and (b) corresponds to *H and *CH_3 adsorbed on a unique surface oxygen atom. Electronic barriers (kJ mol^{-1}) are reported relative to the corresponding bare surface and gas phase alkane. Linear regressions with their corresponding R^2 values are also provided. Linear regressions with their corresponding R^2 fit values are provided for each correlation. (For interpretation of the references to colour in this figure legend, the reader is referred to the web version of this article.)

other steps in ODH (e.g., H_2O formation upon lattice oxygen vacancies, alkene vs. CO_x pathways), we have found that dopants modulate surface reactivity in Mg-vanadates by making unreactive O atoms (in undoped surfaces) more reactive upon doping, while already reactive O atoms retain similar reactivity. Thus, the relative energies between reaction steps during ODH of alkanes (e.g., C–H activation, alkene vs. CO_x formation pathways, H_2O evolution from lattice OH_2*, etc.) may change upon doping if the dopant enables unreactive O atoms to mediate pathways in a *distinct* manner than reactive O atoms already do. For example, if relevant transition states in subsequent ODH elementary pathways have geometric requirements that reactive O-atoms in undoped surfaces do not provide, doping may enable otherwise unreactive O atoms to provide such geometric requirements. Future work will explicitly show how other elementary pathways during ODH may be affected upon doping.

4. Conclusions

The role of substitutional dopants (Ni, Cu, and Zn) on the reactivity of Mg-vanadates was explored using DFT+U ($U = 3.0$ eV, for V-atoms) calculations by systematically exchanging lattice Mg atoms on MgV_2O_6, $Mg_2V_2O_7$ (triclinic and monoclinic), and $Mg_3V_2O_8$ surfaces. Mg-vanadates are known as oxidative dehydrogenation (ODH) catalysts, for which alkane dehydrogenation is thought to proceed via rate determining homolytic C–H activation of the alkane. In this work, Ni, Cu, and Zn were selected because they can all adopt the 2^+ oxidation state of Mg while exhibiting different affinities for the one-electron reduction that mediates alkane C–H activations during ODH.

To address the stability of the doped Mg-vanadate surfaces, we calculated cation exchange energies and demonstrated that the exchange energies are weakly sensitive to changes in the Mg:V ratios. Exchange energies, however, become more exothermic with decreasing Mg-coordination number, suggesting that undercoordinated Mg-atoms are easiest to exchange. These undercoordinated Mg atoms mostly reside near the surface of the slab models because the lowest energy facets of Mg-vanadate materials preserve the former tetrahedral VO_4 coordination of V-atoms, but this occurs at the expense of exposing Mg-atoms by breaking former bulk Mg–O bonds. This, in turn, suggest that dopants preferentially reside near the surface of Mg-vanadate materials, where they are closest to reactive O-atoms and thus can modify surface reactivity.

Hydrogen-addition (HAE) and methyl-addition energies (MAE) were used as reactivity probes and were calculated across 11 Mg-vanadate surfaces (3 MgV_2O_6, 3 $Mg_2V_2O_7$ (triclinic), 3 $Mg_2V_2O_7$ (monoclinic), and 2 $Mg_3V_2O_8$) that have 48 crystallographically distinct reaction sites (O-atoms) and 33 symmetrically unique potential dopant locations (Mg-atoms). Considering this configurational space resulted on 324 unique dopant-O atom combinations, per probe (H* or CH_3*). HAE values were found on average to be 92, 56, and 96 kJ mol^{-1} on Ni-, Cu-, and Zn-doped surfaces, respectively. This suggests that Mg-vanadates are more reducible when doped with Cu, consistent with its propensity to incur in one electron reductions. These results were consistent with MAE values, with corresponding average values, respectively, of –37, –74, and –31 for Ni-, Cu-, and Zn-doped surfaces.

The shifts in HAE and MAE, used to compare changes in reactivity relative to the undoped surfaces, were also found to be largest on Cu, followed by Ni, and Zn. For example, average values for shifts in HAE are –2, –39, and 2 kJ mol^{-1} for Ni-, Cu-, and Zn-doped surfaces, with corresponding average shifts in MAE of –4, –41, and 2 kJ mol^{-1}. Altogether, these values suggest that Cu induces the most exothermic shifts in reducibility. When considering the associated shifts in HAE and MAE per O-atom (active sites) on doped surfaces, we found that shifts are generally more exothermic for unreactive sites, suggesting that dopants moderate reactivity by making more reducible O atoms less reactive and less reducible O atoms more reactive.

HAE and MAE reducibility probes correlate with alkane C–H activation barriers and thus C–H transition state energies on doped-surfaces were found to be consistently lower on Cu-doped surfaces, followed by Ni, and Zn. Alkane C–H activation on V_2O_5 and undoped Mg vanadate surfaces generally occur with higher barriers with increasing Mg:V ratios, however, dopants induce larger exothermic shifts in C–H activation barriers also with increasing Mg:V ratios. For example, average shift in C–H activation energies per bulk material for Cu-doped surfaces were –47, –70, –111, and –136 for MgV_2O_6, t-$Mg_2V_2O_7$, m-$Mg_2V_2O_8$, and $Mg_3V_2O_8$, respectively. These results are consistent with the observation that dopants modify the reactivity of Mg-vanadates by increasing the reducibility of former unreactive O atoms, rather than reinforcing the reducibility of most reactive O atoms in undoped surfaces.

Overall, we establish that, when considering the most likely Mg-vanadate facets to be present during ODH chemistry, substitutionally doping with Cu will induce the largest exothermic shifts in rate determining C–H activation barriers, followed by moderate changes with Ni, to negligible changes (if at all) with Zn. These reactivity trends are consistent with reduction potentials of transition metal dopants (Cu> Ni> Zn), suggesting that dopants modify the reactivity of Mg-vanadate catalysts by introducing new reduction centers for alkane C–H activation, as governed by their likelihood to undergo single electron reduction. Ongoing work explores selectivity determining pathways (i.e., toward ethene), which likely involve two electron reduction processes and thus doping might modify reactivity and selectivity to different extents. This, in turn, would inform and rationalize catalyst synthesis efforts to explore specific transition metal dopants for optimizing ethene yield and selectivity on Mg-vanadate surfaces during ODH chemistry.

CRediT authorship contribution statement

Hansel Montalvo-Castro: Writing – original draft, Visualization, Investigation, Formal analysis, Data curation. **Siby Thomas:** Writing – original draft, Formal analysis, Data curation. **Randall J. Meyer:** Writing – review & editing, Supervision, Resources, Project administration, Funding acquisition. **David Hibbitts:** Writing – review & editing, Supervision, Software, Resources, Project administration, Methodology, Investigation, Funding acquisition, Data curation, Conceptualization.

Declaration of competing interest

The authors declare the following financial interests/personal relationships which may be considered as potential competing interests: David Hibbitts reports financial support was provided by Exxon Mobil Technology and Engineering. David Hibbitts reports a relationship with Exxon Mobil Technology and Engineering that includes: funding grants. If there are other authors, they declare that they have no known competing financial interests or personal relationships that could have appeared to influence the work reported in this paper.

Acknowledgements

This work was funded by ExxonMobil Technology and Engineering Company. Computational resources were provided by ExxonMobil, and University of Florida Research Computing.

Appendix A. Supplementary material

Supplementary data to this article can be found online at https://doi.org/10.1016/j.jcat.2025.116313.

Data availability

Data will be made available on request.

References

[1] I.A. Bakare, S.A. Mohamed, S. Al-Ghamdi, S.A. Razzak, M.M. Hossain, H.I. de Lasa, Fluidized bed ODH of ethane to ethylene over VO_x–MoO_x/γ-Al_2O_3 catalyst: desorption kinetics and catalytic activity, Chem. Eng. J. 278 (2015) 207–216, https://doi.org/10.1016/j.cej.2014.09.114.

[2] Z. Zhai, X. Wang, R. Licht, A.T. Bell, Selective oxidation and oxidative dehydrogenation of hydrocarbons on bismuth vanadium molybdenum oxide, J. Catal. 325 (2015) 87–100, https://doi.org/10.1016/j.jcat.2015.02.015.

[3] H.H. Kung, Oxidative dehydrogenation of light (C_2 to C_4) alkanes, in: Advances in Catalysis, Elsevier, 1994: pp. 1–38. doi: 10.1016/S0360-0564(08)60655-0.

[4] P. Deshlahra, E. Iglesia, Reactivity and selectivity descriptors for the activation of C–H bonds in hydrocarbons and oxygenates on metal oxides, J. Phys. Chem. C 120 (2016) 16741–16760, https://doi.org/10.1021/acs.jpcc.6b04604.

[5] P. Tang, Q. Zhu, Z. Wu, D. Ma, Methane activation: the past and future, Energy Environ. Sci. 7 (2014) 2580–2591, https://doi.org/10.1039/C4EE00604F.

[6] E.T.C. Vogt, B.M. Weckhuysen, Fluid catalytic cracking: recent developments on the grand old lady of zeolite catalysis, Chem. Soc. Rev. 44 (2015) 7342–7370, https://doi.org/10.1039/c5cs00376h.

[7] K.M. Sundaram, G.F. Froment, Modeling of thermal cracking kinetics. 3. radical mechanisms for the pyrolysis of simple paraffins, olefins, and their mixtures, Ind. Eng. Chem. Fund. 17 (1978) 174–182, https://doi.org/10.1021/i160067a006.

[8] C. Boyadjian, L. Lefferts, Catalytic oxidative cracking of light alkanes to alkenes, Eur. J. Inorg. Chem. 2018 (2018) 1956–1968, https://doi.org/10.1002/ejic.201701280.

[9] R. Gounder, E. Iglesia, Catalytic hydrogenation of alkenes on acidic zeolites: mechanistic connections to monomolecular alkane dehydrogenation reactions, J. Catal. 277 (2011) 36–45, https://doi.org/10.1016/j.jcat.2010.10.013.

[10] M.J. Burk, R.H. Crabtree, Selective catalytic dehydrogenation of alkanes to alkenes, J. Am. Chem. Soc. 109 (1987) 8025–8032, https://doi.org/10.1021/ja00260a013.

[11] O.O. James, S. Mandal, N. Alele, B. Chowdhury, S. Maity, Lower alkanes dehydrogenation: strategies and reaction routes to corresponding alkenes, Fuel Process. Technol. 149 (2016) 239–255, https://doi.org/10.1016/j.fuproc.2016.04.016.

[12] A. Sattler, M. Paccagnini, E. Gomez, R.J. Meyer, S. Yacob, H. Klutse, M. Caulfield, Y. Gao, Catalytic limitations on alkane dehydrogenation under H_2 deficient

conditions relevant to membrane reactors, Energy Environ. Sci. 15 (2022) 2120–2129, https://doi.org/10.1039/D2EE00568A.

[13] M. Sheintuch, O. Liron, A. Ricca, V. Palma, Propane dehydrogenation kinetics on supported Pt catalyst, Appl. Catal. A: Gen. 516 (2016) 17–29, https://doi.org/10.1016/j.apcata.2016.02.009.

[14] H. Xie, Z. Wu, S.H. Overbury, C. Liang, V. Schwartz, Investigation of the selective sites on graphitic carbons for oxidative dehydrogenation of isobutane, J. Catal. 267 (2009) 158–166, https://doi.org/10.1016/j.jcat.2009.08.005.

[15] D. Padayachee, A.S. Mahomed, S. Singh, H.B. Friedrich, Selected metal oxides for C H bond activation of n-octane and propensity for CO formation: an empirical study, Mol. Catal. 464 (2019) 1–9, https://doi.org/10.1016/j.mcat.2018.12.008.

[16] C.A. Gärtner, A.C. van Veen, J.A. Lercher, Oxidative dehydrogenation of ethane: common principles and mechanistic aspects, ChemCatChem 5 (2013) 3196–3217, https://doi.org/10.1002/cctc.201200966.

[17] V.D.B.C. Dasireddy, S. Singh, H.B. Friedrich, Oxidative dehydrogenation of n-octane using vanadium pentoxide-supported hydroxyapatite catalysts, Appl. Catal. A: Gen. 421–422 (2012) 58–69, https://doi.org/10.1016/j.apcata.2012.01.034.

[18] D. Creaser, B. Andersson, R.R. Hudgins, P.L. Silveston, Transient study of oxidative dehydrogenation of propane, Appl. Catal. A: Gen. 187 (1999) 147–160, https://doi.org/10.1016/S0926-860X(99)00201-X.

[19] E.A. Mamedov, V. Cortés Corberán, Oxidative dehydrogenation of lower alkanes on vanadium oxide-based catalysts. The present state of the art and outlooks, Appl. Catal. A: Gen. 127 (1995) 1–40, https://doi.org/10.1016/0926-860X(95)00056-9.

[20] K. Chen, A. Khodakov, J. Yang, A.T. Bell, E. Iglesia, Isotopic tracer and kinetic studies of oxidative dehydrogenation pathways on vanadium oxide catalysts, J. Catal. 186 (1999) 325–333, https://doi.org/10.1006/jcat.1999.2510.

[21] K. Chen, E. Iglesia, A.T. Bell, Kinetic isotopic effects in oxidative dehydrogenation of propane on vanadium oxide catalysts, J. Catal. 192 (2000) 197–203, https://doi.org/10.1006/jcat.2000.2832.

[22] F. Cavani, N. Ballarini, A. Cericola, Oxidative dehydrogenation of ethane and propane: how far from commercial implementation? Catal. Today 127 (2007) 113–131, https://doi.org/10.1016/j.cattod.2007.05.009.

[23] H. Fu, Z.-P. Liu, Z.-H. Li, W.-N. Wang, K.-N. Fan, Periodic density functional theory study of propane oxidative dehydrogenation over V2O5(001) surface, J. Am. Chem. Soc. 128 (2006) 11114–11123, https://doi.org/10.1021/ja0611745.

[24] T. Blasco, J.M. Lopez-Nieto, Oxidative dyhydrogenation of short chain alkanes on supported vanadium oxide catalysts, Appl. Catal. A: Gen. 157 (1997) 117–142, https://doi.org/10.1016/S0926-860X(97)00029-X.

[25] A. Khodakov, B. Olthof, A.T. Bell, E. Iglesia, Structure and catalytic properties of supported vanadium oxides: support effects on oxidative dehydrogenation reactions, J. Catal. 181 (1999) 205–216, https://doi.org/10.1006/jcat.1998.2295.

[26] Y. Wang, P. Hu, J. Yang, Y.-A. Zhu, D. Chen, C-H bond activation in light alkanes: a theoretical perspective, Chem. Soc. Rev. 50 (2021) 4299–4358, https://doi.org/10.1039/d0cs01262a.

[27] P.Y. Zavalij, M.S. Whittingham, Structural chemistry of vanadium oxides with open frameworks, Acta Crystallogr. B 55 (1999) 627–663, https://doi.org/10.1107/s0108768199004000.

[28] S. Surnev, M.G. Ramsey, F.P. Netzer, Vanadium oxide surface studies, Prog. Surf. Sci. 73 (2003) 117–165, https://doi.org/10.1016/j.progsurf.2003.09.001.

[29] M.D. Argyle, K. Chen, A.T. Bell, E. Iglesia, Effect of catalyst structure on oxidative dehydrogenation of ethane and propane on alumina-supported vanadia, J. Catal. 208 (2002) 139–149, https://doi.org/10.1006/jcat.2002.3570.

[30] E. Thorsteinson, T.P. Wilson, P.H. Kasai, The oxidative dehydrogenation of ethane over catalysts containing mixed oxides of molybdenum and vanadium, J. Catal. 52 (1978) 116–132, https://doi.org/10.1016/0021-9517(78)90128-8.

[31] J. Le Bars, A. Auroux, M. Forissier, J.C. Vedrine, Active Sites of V_2O_5/γ-Al_2O_3Catalysts in the oxidative dehydrogenation of ethane, J. Catal. 162 (1996) 250–259, https://doi.org/10.1006/jcat.1996.0282.

[32] J. Le Bars, J.C. Védrine, A. Auroux, S. Trautmann, M. Baerns, Microcalorimetric and infrared studies of the acid-base properties of V_2O_5/γ-Al_2O_3 catalysts, Appl. Catal. A: Gen. 119 (1994) 341–354, https://doi.org/10.1016/0926-860X(94)85201-4.

[33] J. Santamaría-González, J. Luque-Zambrana, J. Mérida-Robles, P. Maireles-Torres, A. Jiménez-López, Catalytic behavior of vanadium-containing mesoporous silicas in the oxidative dehydrogenation of propane, Catal. Lett. (2012).

[34] X. Gao, M.A. Bañares, I.E. Wachs, Ethane and n-butane oxidation over supported vanadium oxide catalysts: an *in Situ* UV–visible diffuse reflectance spectroscopic investigation, J. Catal. 188 (1999) 325–331, https://doi.org/10.1006/jcat.1999.2647.

[35] K. Chen, S. Xie, A.T. Bell, E. Iglesia, Structure and properties of oxidative dehydrogenation catalysts based on MoO_3/Al_2O_3, J. Catal. 198 (2001) 232–242, https://doi.org/10.1006/jcat.2000.3125.

[36] F. Arena, F. Frusteri, A. Parmaliana, How oxide carriers affect the reactivity of V_2O_5 catalysts in the oxidative dehydrogenation of propane, Springer Science and Business Media LLC. (1999). doi: 10.1023/a:1019074016773.

[37] A. Corma, J.M. López-Nieto, N. Paredes, M. Pérez, Y. Shen, H. Cao, S.L. Suib, Oxidative dehydrogenation of propane over supported-vanadium oxide catalysts, in: New Developments in Selective Oxidation by Heterogeneous Catalysis, Elsevier, 1992: pp. 213–220. doi: 10.1016/S0167-2991(08)61673-0.

[38] M. Martinez-Huerta, X. Gao, H. Tian, I. Wachs, J. Fierro, M. Banares, Oxidative dehydrogenation of ethane to ethylene over alumina-supported vanadium oxide catalysts: relationship between molecular structures and chemical reactivity, Catal. Today 118 (2006) 279–287, https://doi.org/10.1016/j.cattod.2006.07.034.

[39] Z. Wu, H.-S. Kim, P.C. Stair, S. Rugmini, S.D. Jackson, On the structure of vanadium oxide supported on aluminas: UV and visible Raman spectroscopy, UV-visible diffuse reflectance spectroscopy, and temperature-programmed reduction studies, J. Phys. Chem. B 109 (2005) 2793–2800, https://doi.org/10.1021/jp046011m.

[40] F. Klose, T. Wolff, H. Lorenz, A. Seidelmorgenstern, Y. Suchorski, M. Piorkowska, H. Weiss, Active species on γ-alumina-supported vanadia catalysts: nature and reducibility, J. Catal. 247 (2007) 176–193, https://doi.org/10.1016/j.jcat.2007.01.013.

[41] J.M. López Nieto, P. Botella, M.I. Vázquez, A. Dejoz, The selective oxidative dehydrogenation of ethane over hydrothermally synthesised MoVTeNb catalysts, Chem. Commun. (2002) 1906–1907, https://doi.org/10.1039/b204037a.

[42] Y. Chen, B. Yan, Y. Cheng, State-of-the-art review of oxidative dehydrogenation of ethane to ethylene over $MoVNbTeO_x$ catalysts, Catalysts 13 (2023) 204, https://doi.org/10.3390/catal13010204.

[43] A. Erdohelyi, Oxidation of ethane over silica-supported alkali metal vanadate catalysts, J. Catal. 129 (1991) 497–510, https://doi.org/10.1016/0021-9517(91)90052-6.

[44] S. Hikazudani, K. Kikutani, K. Nagaoka, T. Inoue, Y. Takita, Anaerobic oxidation of isobutane, Appl. Catal. A: Gen. 345 (2008) 65–72, https://doi.org/10.1016/j.apcata.2008.04.022.

[45] H.A. Almukhlifi, R.C. Burns, Oxidative dehydrogenation of isobutane to isobutene by pyrovanadates, $M_2V_2O_7$, where M(II) = Mn, Co, Ni, Cu and Zn, and Co_2VO_4 and ZnV_2O_4 the effect of gold nanoparticles, J. Mol. Catal. A Chem. 408 (2015) 26–40, https://doi.org/10.1016/j.molcata.2015.07.010.

[46] P. Rybarczyk, H. Berndt, J. Radnik, M.M. Pohl, O. Buyevskaya, M. Baerns, A. Brückner, The structure of active sites in Me–V–O catalysts (Me = Mg, Zn, Pb) and its influence on the catalytic performance in the oxidative dehydrogenation (ODH) of propane, J. Catal. 202 (2001) 45–58, https://doi.org/10.1006/jcat.2001.3251.

[47] C. Resini, F. Milella, G. Busca, A study of some bivalent metal divanadates and their catalytic activity in the oxidation of propane, Phys. Chem. Chem. Phys. 2 (2000) 2039–2045, https://doi.org/10.1039/b000447m.

[48] O.S. Owen, H.H. Kung, Effect of cation reducibility on oxidative dehydrogenation of butane on orthovanadates, J. Mol. Catal. 79 (1993) 265–284, https://doi.org/10.1016/0304-5102(93)85107-5.

[49] J. Castiglioni, P. Poix, R. Kieffer, Oxidative dehydrogenation of propane in presence of rare earth vanadates, in: New Frontiers in Catalysis - Proceedings of the 10th International Congress on Catalysis, Budapest, 19-24 July 1992, Elsevier, 1993: pp. 2309–2312. doi: 10.1016/S0167-2991(08)64287-1.

[50] P.M. Michalakos, M.C. Kung, I. Jahan, H. Kung, Selectivity patterns in alkane oxidation over $Mg_3(VO_4)_2$-MgO, $Mg_2V_2O_7$, and $(VO)_2P_2O_7$, J. Catal. 140 (1993) 226–242, https://doi.org/10.1006/jcat.1993.1080.

[51] H. Montalvo-Castro, Á. Loaiza-Orduz, R.J. Meyer, C. Plaisance, D. Hibbitts, Electronic and geometric features controlling the reactivity of Mg-vanadate and V_2O_5 surfaces toward the initial C–H activation of C_1–C_3 alkanes – a DFT+U study, J. Catal. 442 (2025) 115800, https://doi.org/10.1016/j.jcat.2024.115800.

[52] D. Siew Hew Sam, V. Soenen, J.C. Volta, Oxidative dehydrogenation of propane over VMgO catalysts, J. Catal. 123 (1990) 417–435, https://doi.org/10.1016/0021-9517(90)90139-B.

[53] M. Chaar, Selective oxidative dehydrogenation of propane over VMgO catalysts, J. Catal. 109 (1988) 463–467, https://doi.org/10.1016/0021-9517(88)90226-6.

[54] M. Chaar, Selective oxidative dehydrogenation of butane over VMgO catalysts, J. Catal. 105 (1987) 483–498, https://doi.org/10.1016/0021-9517(87)90076-5.

[55] M. Kung, Oxidative dehydrogenation of cyclohexane over vanadate catalysts, J. Catal. 128 (1991) 287–291, https://doi.org/10.1016/0021-9517(91)90084-H.

[56] L. Late, Kinetics of the oxidative dehydrogenation of propane over a VMgO catalyst, J. Nat. Gas Chem. (2002).

[57] A. Burrows, C.J. Kiely, J. Perregaard, P.E. Højlund-Nielsen, G. Vorbeck, J.J. Calvino, C. López-Cartes, Structural Characterisation of a VMgO Catalyst used in the Oxidative Dehydrogenation of Propane, Springer Science and Business Media LLC. (1999). doi: 10.1023/a:1019035229609.

[58] M.C. Kung, K.T. Nguyen, D. Patel, H.H. Kung, Selective Oxidative Dehydrogenation of Light Alkanes over Vanadate Catalysts, in: D.W. Blackburn (Ed.), Catalysis of Organic Reactions, CRC Press, 2020: pp. 289–300. doi: 10.1201/9781003066446-24.

[59] H.H. Kung, M.C. Kung, Oxidative dehydrogenation of alkanes over vanadium-magnesium-oxides, Appl. Catal. A: Gen. 157 (1997) 105–116, https://doi.org/10.1016/S0926-860X(97)00028-8.

[60] S. Zhang, H. Liu, Insights into the structural requirements for oxidative dehydrogenation of propane on crystalline Mg-V-O catalysts, Appl. Catal. A: Gen. 568 (2018) 1–10, https://doi.org/10.1016/j.apcata.2018.09.019.

[61] S. Sugiyama, T. Hashimoto, Y. Tanabe, N. Shigemoto, H. Hayashi, Effects of the enhancement of the abstraction of lattice oxygen from magnesium vanadates incorporated with copper(II) cations on the oxidative dehydrogenation of propane, J. Mol. Catal. A Chem. 227 (2005) 255–261, https://doi.org/10.1016/j.molcata.2004.10.046.

[62] Y. Liu, L. Annamalai, P. Deshlahra, Effects of lattice O atom coordination and pore confinement on selectivity limitations for ethane oxidative dehydrogenation catalyzed by vanadium-oxo species, J. Phys. Chem. C 123 (2019) 28168–28191, https://doi.org/10.1021/acs.jpcc.9b07778.

[63] V. Fung, F. (Feng) Tao, D. Jiang, Trends of alkane activation on doped cobalt (II, III) oxide from first principles, ChemCatChem 10 (2018) 244–249, https://doi.org/10.1002/cctc.201700960.

[64] C. Tan, H. Liu, Y. Qin, L. Li, H. Wang, X. Zhu, Q. Ge, Correlation between the properties of surface lattice oxygen on NiO and its reactivity and selectivity towards the oxidative dehydrogenation of propane, ChemPhysChem (2022) e202200539, https://doi.org/10.1002/cphc.202200539.

[65] V. Shapovalov, H. Metiu, Catalysis by doped oxides: CO oxidation by $Au_xCe_{1-x}O_2$, J. Catal. 245 (2007) 205–214, https://doi.org/10.1016/j.jcat.2006.10.009.

[66] P. Singh, A. Gogoi, Q.U. Aien, M. Dixit, Assessing the effect of dopants on the C-H activation activity of γ-Al_2O_3 using first-principles calculations, ChemPhysChem 24 (2023) e202200670, https://doi.org/10.1002/cphc.202200670.

[67] T. Vinodkumar, B.G. Rao, B.M. Reddy, Influence of isovalent and aliovalent dopants on the reactivity of cerium oxide for catalytic applications, Catal. Today 253 (2015) 57–64, https://doi.org/10.1016/j.cattod.2015.01.044.

[68] G. Parravano, The catalytic oxidation of carbon monoxide on nickel oxide. I. pure nickel oxide, J. Am. Chem. Soc. 75 (1953) 1448–1451, https://doi.org/10.1021/ja01102a050.

[69] Z.-P. Liu, P. Hu, General rules for predicting where a catalytic reaction should occur on metal surfaces: a density functional theory study of C-H and C-O bond breaking/making on flat, stepped, and kinked metal surfaces, J. Am. Chem. Soc. 125 (2003) 1958–1967, https://doi.org/10.1021/ja0207551.

[70] M.D. Krcha, A.D. Mayernick, M.J. Janik, Periodic trends of oxygen vacancy formation and C–H bond activation over transition metal-doped CeO_2 (111) surfaces, J. Catal. 293 (2012) 103–115, https://doi.org/10.1016/j.jcat.2012.06.010.

[71] B. Li, H. Metiu, Dissociation of methane on La_2O_3 surfaces doped with Cu, Mg, or Zn, J. Phys. Chem. C 115 (2011) 18239–18246, https://doi.org/10.1021/jp2049603.

[72] W. Tang, Z. Hu, M. Wang, G.D. Stucky, H. Metiu, E.W. McFarland, Methane complete and partial oxidation catalyzed by Pt-doped CeO_2, J. Catal. 273 (2010) 125–137, https://doi.org/10.1016/j.jcat.2010.05.005.

[73] H. Zhu, D.C. Rosenfeld, M. Harb, D.H. Anjum, M.N. Hedhili, S. Ould-Chikh, J.-M. Basset, Ni–M–O (M = Sn, Ti, W) catalysts prepared by a dry mixing method for oxidative dehydrogenation of ethane, ACS Catal. 6 (2016) 2852–2866, https://doi.org/10.1021/acscatal.6b00044.

[74] I. Popescu, E. Heracleous, Z. Skoufa, A. Lemonidou, I.-C. Marcu, Study by electrical conductivity measurements of semiconductive and redox properties of M-doped NiO (M = Li, Mg, Al, Ga, Ti, Nb) catalysts for the oxidative dehydrogenation of ethane, Phys. Chem. Chem. Phys. 16 (2014) 4962–4970, https://doi.org/10.1039/c3cp54817a.

[75] B.G. Ershov, Estimation of the reduction potential of transition metal atoms in aqueous solutions, J. Mol. Liq. 390 (2023) 123129, https://doi.org/10.1016/j.molliq.2023.123129.

[76] G. Kresse, J. Hafner, *Ab initio* molecular dynamics for liquid metals, Phys. Rev. B 47 (1993) 558–561, https://doi.org/10.1103/PhysRevB.47.558.

[77] G. Kresse, J. Hafner, *Ab initio* molecular-dynamics simulation of the liquid-metal–amorphous-semiconductor transition in germanium, Phys. Rev. B 49 (1994) 14251–14269, https://doi.org/10.1103/PhysRevB.49.14251.

[78] P. Kravchenko, C. Plaisance, D. Hibbitts, A new computational interface for catalysis, Published as pre-print on doi: 10.26434/chemrxiv.8040737.v4 (2019). doi: 10.26434/chemrxiv.8040737.v3.

[79] G. Kresse, J. Furthmüller, Efficient iterative schemes for *ab initio* total-energy calculations using a plane-wave basis set, Phys. Rev. B 54 (1996) 11169–11186, https://doi.org/10.1103/PhysRevB.54.11169.

[80] G. Kresse, J. Furthmüller, Efficiency of ab-initio total energy calculations for metals and semiconductors using a plane-wave basis set, Comp. Mater. Sci. 6 (1996) 15–50, https://doi.org/10.1016/0927-0256(96)00008-0.

[81] J.P. Perdew, K. Burke, M. Ernzerhof, Generalized gradient approximation made simple, Phys. Rev. Lett. 77 (1996) 3865–3868, https://doi.org/10.1103/PhysRevLett.77.3865.

[82] L. Wang, T. Maxisch, G. Ceder, Oxidation energies of transition metal oxides within the GGA+U framework, Phys. Rev. B 73 (2006) 195107, https://doi.org/10.1103/PhysRevB.73.195107.

[83] V.I. Anisimov, O. Gunnarsson, Density-functional calculation of effective Coulomb interactions in metals, Phys. Rev. B Condens. Matter 43 (1991) 7570–7574, https://doi.org/10.1103/physrevb.43.7570.

[84] J.F. Herbst, R.E. Watson, J.W. Wilkins, Relativistic calculations of 4f excitation energies in the rare-earth metals: further results, Phys. Rev. B 17 (1978) 3089–3098, https://doi.org/10.1103/PhysRevB.17.3089.

[85] S.A. Tolba, K.M. Gameel, B.A. Ali, H.A. Almossalami, N.K. Allam, The DFT+U: approaches, accuracy, and applications, in: G. Yang (Ed.), Density Functional Calculations - Recent Progresses of Theory and Application, InTech, (2018). doi: 10.5772/intechopen.72020.

[86] H.H. Kristoffersen, H. Metiu, Reconstruction of low-index α-V_2O_5 surfaces, J. Phys. Chem. C 119 (2015) 10500–10506, https://doi.org/10.1021/acs.jpcc.5b02383.

[87] R. Defrance, B. Sklénard, M. Guillaumont, J. Li, M. Freyss, Ab initio study of electron mobility in VO via polaron hopping, Solid State Electron. 198 (2022) 108455, https://doi.org/10.1016/j.sse.2022.108455.

[88] T. Das, S. Tosoni, G. Pacchioni, Structural and electronic properties of bulk and ultrathin layers of V_2O_5 and MoO_3, Comp. Mater. Sci. 163 (2019) 230–240, https://doi.org/10.1016/j.commatsci.2019.03.027.

[89] W. Song, T. Liu, L. Yang, J. Jiang, Thermodynamics of native defects in V_2O_5 crystal: a first-principles method, Comp. Mater. Sci. 220 (2023) 112071, https://doi.org/10.1016/j.commatsci.2023.112071.

[90] Y. Liu, Q. Hu, D. Ma, X. Liu, Z. You, G. Qiu, X. Lv, Periodic DFT study on the adsorption and deoxygenation process of NH_3 on V_2O_5 (001) surface, JOM 74 (2022) 1870–1877, https://doi.org/10.1007/s11837-022-05256-6.

[91] V.A. Ranea, P.L. Dammig Quiña, N.M. Yalet, General adsorption model for H_2S, H_2Se, H_2Te, NH_3, PH_3, AsH_3 and SbH_3 on the V_2O_5(001) surface including the van der Waals interaction, Chem. Phys. Lett. 720 (2019) 58–63, https://doi.org/10.1016/j.cplett.2019.02.013.

[92] D. Koch, S. Manzhos, Interstitial versus substitutional metal insertion in V_2O_5 as post-lithium ion battery cathode: a comparative GGA/GGA+U study with localized bases, MRS Commun. 10 (2020) 259–264, https://doi.org/10.1557/mrc.2020.36.

[93] N.M. Yalet, V.A. Ranea, A DFT+U study on the adsorption of CO, H_2S, PH_3, CO_2 and SO_2 on the V_2O_5(001) surface with atomic Rh adsorbed, Surf. Sci. 718 (2022) 122014, https://doi.org/10.1016/j.susc.2021.122014.

[94] G. Kumar, S.L.J. Lau, M.D. Krcha, M.J. Janik, Correlation of methane activation and oxide catalyst reducibility and its implications for oxidative coupling, ACS Catal. 6 (2016) 1812–1821, https://doi.org/10.1021/acscatal.5b02657.

[95] E. Sargeant, F. Illas, P. Rodríguez, F. Calle-Vallejo, Importance of the gas-phase error correction for O_2 when using DFT to model the oxygen reduction and evolution reactions, J. Electroanal. Chem. 896 (2021) 115178, https://doi.org/10.1016/j.jelechem.2021.115178.

[96] M.O. Almeida, M.J. Kolb, M.R.V. Lanza, F. Illas, F. Calle-Vallejo, Gas-phase errors affect dft-based electrocatalysis models of oxygen reduction to hydrogen peroxide, ChemElectroChem 9 (2022), https://doi.org/10.1002/celc.202200210.

[97] J.K. Nørskov, J. Rossmeisl, A. Logadottir, L. Lindqvist, J.R. Kitchin, T. Bligaard, H. Jónsson, Origin of the overpotential for oxygen reduction at a fuel-cell cathode, J. Phys. Chem. B 108 (2004) 17886–17892, https://doi.org/10.1021/jp047349j.

[98] A.B. Anderson, E.F. Holby, Pathways for O_2 electroreduction over substitutional FeN_4, $HOFeN_4$, and $OFeN_4$ in graphene bulk sites: critical evaluation of overpotential predictions using LGER and CHE models, J. Phys. Chem. C 123 (2019) 18398–18409, https://doi.org/10.1021/acs.jpcc.9b03703.

[99] H. Jónsson, G. Mills, K.W. Jacobsen, Nudged elastic band method for finding minimum energy paths of transitions, in: B.J. Berne, G. Ciccotti, D.F. Coker (Eds.), Classical and Quantum Dynamics in Condensed Phase Simulations, World Scientific, 1998, pp. 385–404, https://doi.org/10.1142/9789812839664_0016.

[100] G. Henkelman, B.P. Uberuaga, H. Jónsson, A climbing image nudged elastic band method for finding saddle points and minimum energy paths, J. Chem. Phys. 113 (2000) 9901–9904, https://doi.org/10.1063/1.1329672.

[101] G. Henkelman, H. Jónsson, Improved tangent estimate in the nudged elastic band method for finding minimum energy paths and saddle points, J. Chem. Phys. 113 (2000) 9978–9985, https://doi.org/10.1063/1.1323224.

[102] G. Henkelman, H. Jónsson, A dimer method for finding saddle points on high dimensional potential surfaces using only first derivatives, J. Chem. Phys. 111 (1999) 7010–7022, https://doi.org/10.1063/1.480097.

[103] A.D. Mayernick, M.J. Janik, Methane activation and oxygen vacancy formation over CeO_2 and Zr, Pd substituted CeO_2 surfaces, J. Phys. Chem. C 112 (2008) 14955–14964, https://doi.org/10.1021/jp805134s.

[104] A. Cherrak, R. Hubaut, Y. Barbaux, G. Mairesse, Catalytic properties of bismuth vanadates based catalysts in oxidative coupling of methane and oxidative dehydrogenation of propane, Catal. Lett. 15 (1992) 377–383, https://doi.org/10.1007/BF00769161.